LETTER

doi:10.1038/nature13852

Luminal signalling links cell communication to tissue architecture during organogenesis

Sevi Durdu[1], Murat Iskar[1], Celine Revenu[1]†, Nicole Schieber[1], Andreas Kunze[1], Peer Bork[1], Yannick Schwab[1] & Darren Gilmour[1]

Morphogenesis is the process whereby cell collectives are shaped into differentiated tissues and organs[1]. The self-organizing nature of morphogenesis has been recently demonstrated by studies showing that stem cells in three-dimensional culture can generate complex organoids, such as mini-guts[2], optic-cups[3] and even mini-brains[4]. To achieve this, cell collectives must regulate the activity of secreted signalling molecules that control cell differentiation, presumably through the self-assembly of microenvironments or niches. However, mechanisms that allow changes in tissue architecture to feedback directly on the activity of extracellular signals have not been described. Here we investigate how the process of tissue assembly controls signalling activity during organogenesis *in vivo*, using the migrating zebrafish lateral line primordium[5]. We show that fibroblast growth factor (FGF) activity within the tissue controls the frequency at which it deposits rosette-like mechanosensory organs. Live imaging reveals that FGF becomes specifically concentrated in microluminal structures that assemble at the centre of these organs and spatially constrain its signalling activity. Genetic inhibition of microlumen assembly and laser micropuncture experiments demonstrate that microlumina increase signalling responses in participating cells, thus allowing FGF to coordinate the migratory behaviour of cell groups at the tissue rear. As the formation of a central lumen is a self-organizing property of many cell types, such as epithelia[6] and embryonic stem cells[7], luminal signalling provides a potentially general mechanism to locally restrict, coordinate and enhance cell communication within tissues.

A major challenge in biology is to explain how the pattern of complex organs emerges through dynamic self-organizing processes occurring at cellular and molecular scales[1,8,9]. The development of the zebrafish posterior lateral line system provides an example of an *in vivo* organogenesis process that has the potential to be understood quantitatively at subcellular resolution[10]. Here, a series of rosette-like mechanosensory organs is assembled and deposited along the flanks of the embryo by a collectively migrating epithelial primordium[5]. While a number of signalling pathways required for this process have been identified[11], it is currently not known how their activity is coupled to this organogenesis process. We therefore first performed a quantitative analysis of the normal organ deposition process by time-lapse imaging of many wild-type (WT) embryos (Fig. 1a and Supplementary Videos 1 and 2). This revealed that the overall pattern of organ spacing is determined by the timing of deposition events, rather than by sustained changes in the speed of primordium migration or growth of the embryo (Fig. 1b and Extended Data Fig. 1).

The best candidate regulator of this organ deposition process is FGF signalling, as FGF ligands have been shown to be required for organ formation[12–14]. To test if this pathway controls organ deposition timing we reduced its activity in a stepwise manner, by titrating the FGF receptor inhibitor SU5402 (ref. 12). This showed that reducing FGF activity results in a dose-dependent delay in organ deposition (Fig. 1c, Extended Data Fig. 2 and Supplementary Video 3), a finding we confirmed using mutants for Fgfr1a[15], the receptor that mediates signalling in this context (Extended Data Fig. 2 and Supplementary Video 4). Conversely, when we increased the concentration of FGF-ligand, by expressing a progesterone-inducible transcription factor[16] (*cxcr4b:lexPR*) that drives uniform overexpression of a functional fusion protein of Fgf3 and green fluorescent protein (*lexOP:fgf3–GFP*), organ deposition was accelerated in a dose-dependent manner (Fig. 1d, Extended Data Fig. 2 and Supplementary Video 5). Uniform overexpression of Fgf3–GFP did not significantly alter rosette-like organ assembly rate, indicating that its effect was primarily on the migratory behaviour of assembled organs (Extended Data Fig. 3). Thus, the timing of this organ deposition process can be controlled over a wide dynamic range by the activity level of a single signalling molecule.

Since FGF regulates lateral line organ deposition in a dose-dependent manner, its extracellular concentration and distribution must be tightly controlled. Imaging the FGF distribution after uniform overexpression

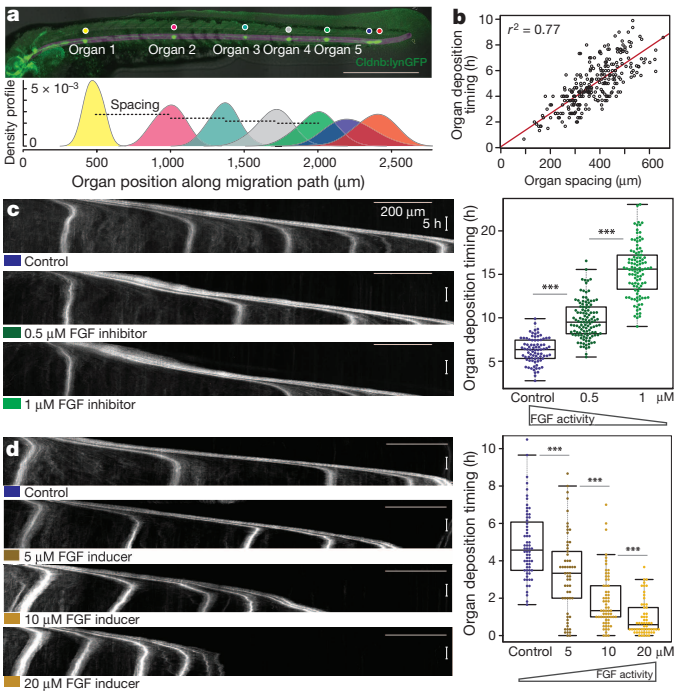

Figure 1 | FGF signalling regulates organ deposition timing in a dose-dependent manner. **a**, Quantitative analysis of lateral line patterning. Position of organs along lateral line at 2 days post-fertilization (d.p.f.) (*cldnb:lynGFP*). Plot shows intensity profile of pooled organ positions (below, $N = 60$ (throughout, N represents number of embryos and n represents data points)). Organs and migrating primordium are colour-coded. **b**, Correlation of organ deposition timing and spacing between consecutive depositions (Spearman $r^2 = 0.77$, $n = 260$). **c**, **d**, Influence of FGF level on organ deposition. **c**, Kymographs of control, 0.5 μM and 1 μM SU5402-treated samples. Plot shows quantification of organ deposition timing ($n = 82, 114, 104$). **d**, Kymographs of control, 5, 10 and 20 μM RU486-treated samples and plots of organ deposition timing ($n = 64, 57, 65, 58$). Scale bars, 500 μm (**a**), 200 μm, 5 h (**c**, **d**). Statistics: Wilcoxon, $***P < 0.001$.

[1]European Molecular Biology Laboratory Heidelberg, Meyerhofstrasse 1, 69117 Heidelberg, Germany. †Present address: Institut Curie, 26 rue d'Ulm, 75248 Paris, France.

©2014 Macmillan Publishers Limited. All rights reserved

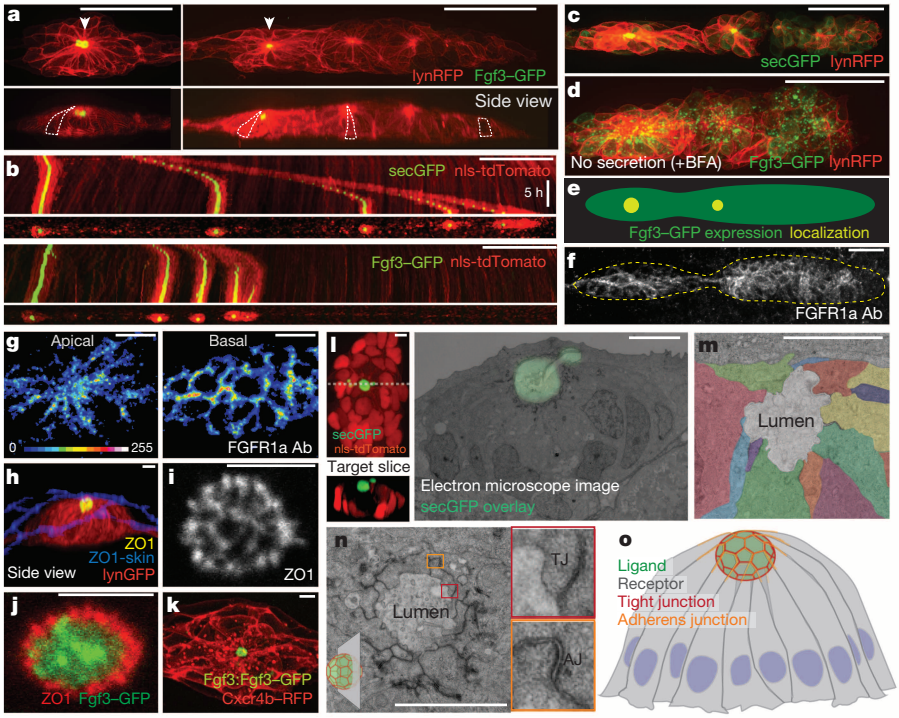

Figure 2 | Secreted FGF becomes concentrated in multicellular microlumina at the centre of organ progenitors. Fgf3–GFP and secGFP images are taken from stable LexOP lines unless otherwise stated. **a**, Fgf3–GFP localizes to apical spheres (arrowheads) after uniform expression (red membrane counter-label, cells outlined in dashed lines in side view). **b**, Kymographs showing that the appearance of Fgf3–GFP and secGFP accumulation correlates with onset of organ deposition. **c**, secGFP localization in primordium. **d**, Intracellular accumulation of Fgf3–GFP vesicles after brefeldin A (+BfA) treatment. **e**, Schema comparing expression (green) and localization (yellow) patterns of Fgf3–GFP. **f**, Fgfr1a protein distribution (anti-Fgfr1a antibody) in migrating primordium. **g**, Anti-Fgfr1a antibody staining in apical and basal optical slices of a rear rosette (calibration bar: signal intensity). **h**, **i**, Tight junction 'bucky ball' in deposited organs (yellow) and tight junctions of overlying skin cells (blue). **i**, Higher-resolution view of **h**. **j**, Co-labelling of Fgf3–GFP (green) and tight junctions (ZO1, red). **k**, BAC *fgf3:Fgf3–GFP* embryo shows microluminal localization, membranes labelled with BAC *cxcr4b:Cxcr4b–RFP* (RFP, red fluorescent protein). **l**–**n**, CLEM analysis of microlumen. **l**, Fluorescent images used for CLEM alignment showing slice position (dashed), orthogonal view (below), secGFP and electron microscope overlay at same position (right). **m**, Plasma membrane tracking shows microlumina is assembled form many cells (pseudocoloured). **n**, Microluminal space and surrounding cell junctions (schematic: section position), boxes show higher-resolution view (red, tight junctions (TJ); orange, adherens junctions (AJ)). **o**, Schematic representation of organ with central microlumen. Scale bars, 50 μm (**a**, **c**, **d**), 200 μm, 5 h (**b**), 20 μm (**f**), 5 μm (**g**, **h**, **i**, **j**, **k**, **l**, **m**, **n**).

of Fgf3–GFP revealed that it was concentrated in spherical volumes at the apical centre of organ progenitor rosettes (Fig. 2a, e). Time-lapse analysis showed that the appearance of these spheres correlated with the deceleration and arrest of the associated organ progenitor (Fig. 2b and Supplementary Video 6). Apical spheres were also observed when the tissue expressed a secreted form of GFP (secGFP; Fig. 2b, c). Inhibiting protein secretion with brefeldin A prevented Fgf3–GFP localization to these apical spheres and retained it in vesicles within all cells of the primordium (Fig. 2d), indicating that these spheres represent tightly restricted pools of apically secreted proteins (Extended Data Fig. 4). By contrast, direct visualization of endogenous Fgfr1a, using a newly generated monoclonal antibody against the zebrafish protein, revealed an unrestricted plasma membrane distribution of the receptor (Fig. 2f, g). Immunofluorescence of tight-junctions[17] (Fig. 2h–j) and ultrastructural analysis using correlative light electron microscopy (CLEM; Fig. 2l–n and Extended Data Fig. 5)[18] demonstrated that these apical spheres of secreted protein represent extracellular pockets, or microlumina, assembled from cell apical domains and displaying the cell junctions characteristic of a lumen (Fig. 2n, o and Extended Data Fig. 5). Identical luminal localization was also observed when Fgf3–GFP was expressed at normal physiological levels using BAC-mediated complementation (*fgf3:fgf3–GFP*; Fig. 2k and Extended Data Fig. 6). Interestingly, these microlumina showed a geodesic organization to which each cell of the organ progenitor contributes a facet and thus has access to this shared microenvironment (Fig. 2m, o). The secGFP signal correlated perfectly with the shape of the luminal cavity, even filling 'side-pockets' that are formed stochastically by protruding sensory kinocilia of differentiating organs (Fig. 2l, Extended Data Fig. 5 and Supplementary Video 7), suggesting that secreted proteins freely diffuse within the microlumen. Indeed, fluorescence loss in photobleaching (FLIP) and fluorescence recovery after photobleach (FRAP) analysis of Fgf3–GFP confirmed that Fgf3–GFP is highly mobile within the microlumen (Extended Data Fig. 5).

The results described above reveal that microlumina could act as 'hubs' that locally concentrate secreted FGF molecules and ensure coordinated signalling responses within the migrating tissue. Alternatively, signalling activity may be determined by concentration gradients of freely diffusible FGF molecules in the open extracellular environment, consistent with its known role as a morphogen in other contexts[19]. To distinguish between these two models (Fig. 3a), we investigated the range of FGF action by overexpressing the protein from randomly positioned cell clones that were generated either by cell transplantation (Fig. 3b and Extended Data Fig. 7) or mosaic expression of *lexOP:fgf3–GFP* (Fig. 3d). Interestingly, Fgf3–GFP was secreted into microlumina independently of the position of the expressing cell within the rosette, indicating that any cell of the group can contribute signal to the microluminal pool (Fig. 3c and Extended Data Fig. 7). As a first readout of FGF activity, we mapped the deposition intervals of organs with and without ectopic Fgf3–GFP-expressing cells. As shown in Fig. 3, individual ectopic Fgf3–GFP-expressing cells efficiently arrested the migration of cells that were connected to the same Fgf3–GFP-positive microlumen but they had no effect on cells in neighbouring organs, even when they were physically closer than cells of the same organ (Fig. 3b, d, Extended Data Fig. 7 and Supplementary Video 8). Thus, the organ deposition response to ectopic

©2014 Macmillan Publishers Limited. All rights reserved

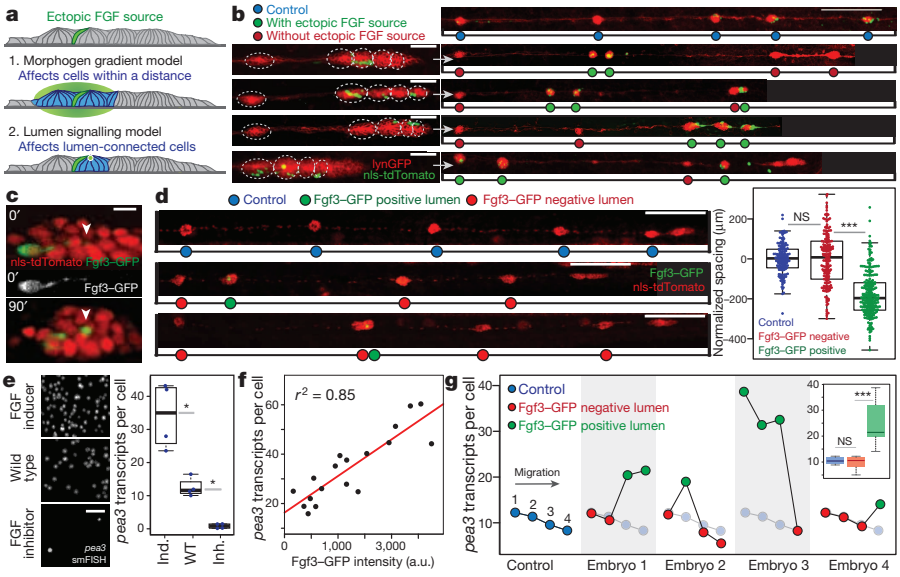

Figure 3 | Microlumina focus FGF-signalling activity within migrating collective. **a**, Schema showing possible outcomes of ectopic FGF experiments. **b**, *lexOP:Fgf3–GFP/cxcr4b:nls-tdTomato* cell clones (green) transplanted into *cldnb:lynGFP* primordium (red), showing future organ territories (dashed line) and final pattern of organ deposition (right). **c**, Time-lapse of microluminal filling by single Fgf3–GFP cell after drug induction in mosaic tissue (arrow heads pointing organ centre). **d**, Organ deposition pattern after mosaic *lexOP:fgf3–GFP* (green) expression by transient injection. Box-plot of organ spacing in mosaic embryos with Fgf3–GFP-positive microlumen (green, $n = 240$), without Fgf3–GFP-positive microlumen (red, $n = 170$) and control injections (blue, $n = 141$), normalized by mean interval values of controls. **e**, Magnified views of *pea3* smFISH in WT, FGF inducer- (Ind.; 15 μM RU486) and FGF inhibitor- (Inh.; 4 μM SU5402) treated primordia, as segmented images. Quantification of *pea3* transcripts per cell (tissue $N = 4, 4, 4$, approximately 160 cells per tissue). **f**, Correlation of luminal Fgf3–GFP intensity and *pea3* transcript counts achieved by titration of inducer (Spearman $r^2 = 0.85$, $n = 18$); a.u., arbitrary units. **g**, *pea3* smFISH in Fgf3–GFP-positive and -negative organs. Only Fgf3–GFP-positive organs show higher *pea3* transcript levels per cell. Scale bars, 50 μm (**b** left), 200 μm (**b** right, **d**), 10 μm (**c**), 2 μm (**e**). Statistics: Wilcoxon. NS, not significant; $*P < 0.05$; $***P < 0.001$.

FGF activity was local and coordinated, affecting only cells that shared a microlumen with Fgf3–GFP source cells. To measure FGF signalling more directly, we next monitored the transcription of its immediate target gene *pea3* (ref. 20) by single-molecule fluorescent *in situ* hybridization approach (smFISH), which revealed a clear Fgf-dependent response (Fig. 3e, f, Extended Data Fig. 8 and Supplementary Video 9). *Pea3* smFISH analysis of primordia carrying ectopic Fgf3–GFP-expressing clones showed that all cells in contact with Fgf3–GFP-positive microlumina upregulated target gene transcription, whereas cells from neighbouring rosettes showed no change (Fig. 3g), confirming that the response to FGF signalling is highly restricted. In addition, this revealed that upregulated FGF signalling responses were uniform across individual organ precursors. In conclusion, single-cell ectopic expression of FGF does not support a model where FGF responses are determined by a concentration gradient diffusing from secreting cells. By contrast, these data are fully consistent with the model where the FGF signal is locally concentrated, and collectively presented, by a central microlumen. Thus, the formation of microlumen allows FGF signalling, widely studied for its role in mediating long-range positional information[19], to coordinate locally the behaviour of discrete cell groups within the migrating tissue.

The luminal signalling model predicts that these multicellular assemblies are required for efficient FGF signalling responses. To test this, we first applied a genetic method to prevent microluminal assembly, an approach complicated by the fact that many key regulators of this process also control epithelial polarity[21,22]. We therefore knocked down shroom3, an actin-binding[23] protein required for apical constriction of organ progenitor cells but not for epithelial polarity[24]. Morpholino knockdown of shroom3 transiently suppressed microluminal formation, as revealed by a failure to concentrate secGFP (Fig. 4a). smFISH analysis of *pea3* confirmed that FGF target gene transcription was significantly reduced (Fig. 4b). Second, we acutely opened microlumen structures by two-photon laser micropuncture, which caused rapid leakage of Fgf3–GFP (Fig. 4c, d, Extended Data Fig. 9 and Supplementary Video 10), confirming that these local build-ups of FGF signal are dependent on microlumen integrity. The microluminal opening by laser micropuncture was transient, as revealed by the recovery of characteristic microluminal Fgf3–GFP spheres, showing that this targeted perturbation had negligible effects on cell viability (Extended Data Fig. 9). Nevertheless, smFISH analysis of *pea3* revealed that target gene expression was reduced after transient depletion of microluminal Fgf3–GFP, demonstrating that trapping of secreted FGF is required to maintain high signalling levels (Fig. 4e). In addition, microluminal opening specifically delayed the deposition of targeted organs by prolonging their migration, a direct confirmation that microlumina are required for FGF to exert its biological role during this organogenesis process (Fig. 4f). Finally, we exploited the fact that the microluminal cavity is opened when deposited organ progenitors fuse with the overlying skin, a natural event that also leads to rapid loss of Fgf3–GFP (Extended Data Fig. 10). Since the timing of skin fusion varies between embryos, we could directly compare organs where microlumina had just opened with those that were still closed at identical developmental stages (Fig. 4g, Supplementary Video 6). smFISH analysis of *pea3* in this unperturbed context revealed that FGF signalling was again reduced specifically in organs with opened microlumina (Fig. 4g). Combined, these data provide compelling experimental support for a model where microlumina act as shared microenvironments that locally concentrate FGF to enhance signalling within the migrating tissue (Fig. 4h).

Previous studies addressing the regulation of extracellular signals have focused on the role of additional cell surface or extracellular proteins, such as heparan sulphate proteoglycans[25] and receptors[26], whose own spatiotemporal regulation is currently under investigation[27]. Here, we uncover an alternative mechanism that instead exploits an intrinsic biological feature of epithelial tissues, namely their ability to assemble a shared enclosed lumen[6]. This finding has important implications for understanding how responses to extracellular signals are controlled and coordinated in tissues *in vivo*. To our knowledge, it provides the first such mechanism that acts specifically at the level of multicellular organization, as only cell groups that assemble a central lumen are able to trap and concentrate the freely diffusible ligand (Fig. 4h). We propose that formation of the microlumen is required to restrict, coordinate and

©2014 Macmillan Publishers Limited. All rights reserved

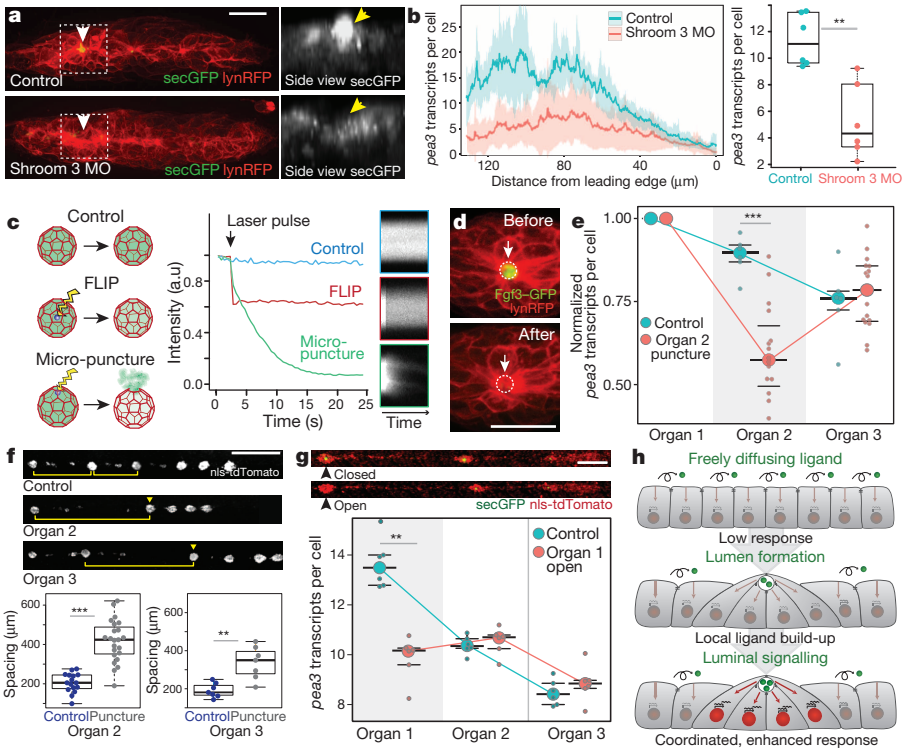

Figure 4 | Microluminal assembly and integrity are required for efficient FGF signalling. **a**, **b**, Knockdown of shroom3 (Shroom3 MO) prevents microlumen formation and leads to lack of apical spheres in *lexOP:secGFP* primordia (**a**, arrowhead), and reduces *pea3* transcription, shown in profile plot and box-plot quantification (**b**, $N = 6, 6$). **c**–**e**, Schema of two-photon micropuncture approach. **c**, Schematic representation of micropuncture experiment (left). Plot of Fgf3–GFP pool fluorescence intensity after micropuncture (green) or internal bleach pulse (red). Panels show kymographs. **d**, Images of Fgf3–GFP-positive organ before and after micropuncture. **e**, *Pea3* smFISH of Fgf3–GFP-expressing organs 30–60 min after micropuncture, comparing organ 2 micropunctured samples (pink, $N = 16$) with controls (blue, $N = 6$). Absolute *pea3* transcripts per cell were normalized to first organ for each embryo. **f**, Organ deposition delay after luminal micropuncture of Fgf3–GFP-expressing second ($n = 16, 23$) and third ($n = 7, 7$) organs. Quantification of organ deposition spacing (bottom). **g**, Comparison of secGFP- (green) expressing primordia (red) in identical stage embryos; lower specimen shows loss of secGFP microlumina in organ 1 after fusion with the overlying skin (arrowhead). smFISH reveals reduced *pea3* transcript levels in opened organs when compared with unopened organs ($N = 6, 6$). **h**, Schematic representation of microlumen signalling model. Scale bars, 20 μm (**a**, **d**), 200 μm (**f**), 100 μm (**g**). Statistics: Wilcoxon. $^{**}P < 0.01$; $^{***}P < 0.001$.

enhance FGF signalling within the migrating tissue. This local increase in FGF activity then positively feedbacks on microlumina by increasing the epithelial character of responding cells, leading to the formation of stable rosettes. Thus, luminal hubs provide a morphogenetic checkpoint function by ensuring, in this case, that cells become polarized and organized before they can respond efficiently to signals promoting their differentiation. Moreover, as lumen formation itself is highly sensitive to changes in epithelial polarity and adhesion[21,28], it is likely that luminal signalling hubs can be rapidly disassembled and reassembled by processes that alter cell cohesion, such as the epithelial–mesenchymal transition that is a hallmark of organogenesis and cancer[29]. However, this mechanism could potentially be active in any context where cells construct a lumen or similar enclosed extracellular microenvironment, such as the transient tissue-folds that are prevalent during morphogenesis[30]. A notable example is provided by the recent finding that early mammalian embryos and embryonic stem cells self-organize to form polarized rosettes with a central lumen[7], structures that are morphologically highly similar to those interrogated here. Our study suggests potential signalling roles for shared lumina in many other tissue contexts.

Online Content Methods, along with any additional Extended Data display items and Source Data, are available in the online version of the paper; references unique to these sections appear only in the online paper.

Received 15 April; accepted 9 September 2014.
Published online 22 October 2014.

1. Sasai, Y. Cytosystems dynamics in self-organization of tissue architecture. *Nature* **493,** 318–326 (2013).
2. Sato, T. & Clevers, H. Growing self-organizing mini-guts from a single intestinal stem cell: mechanism and applications. *Science* **340,** 1190–1194 (2013).
3. Eiraku, M. *et al.* Self-organizing optic-cup morphogenesis in three-dimensional culture. *Nature* **472,** 51–56 (2011).
4. Lancaster, M. A. *et al.* Cerebral organoids model human brain development and microcephaly. *Nature* **501,** 373–379 (2013).
5. Ghysen, A. & Dambly-Chaudière, C. The lateral line microcosmos. *Genes Dev.* **21,** 2118–2130 (2007).
6. O'Brien, L. E., Zegers, M. M. P. & Mostov, K. E. Opinion: building epithelial architecture: insights from three-dimensional culture models. *Nature Rev. Mol. Cell Biol.* **3,** 531–537 (2002).
7. Bedzhov, I. & Zernicka-Goetz, M. Self-organizing properties of mouse pluripotent cells initiate morphogenesis upon implantation. *Cell* **156,** 1032–1044 (2014).
8. Reeves, G. T., Muratov, C. B., Schüpbach, T. & Shvartsman, S. Y. Quantitative models of developmental pattern formation. *Dev. Cell* **11,** 289–300 (2006).
9. Metzger, R. J., Klein, O. D., Martin, G. R. & Krasnow, M. A. The branching programme of mouse lung development. *Nature* **453,** 745–750 (2008).
10. Revenu, C. *et al.* Quantitative cell polarity imaging defines leader-to-follower transitions during collective migration and the key role of microtubule-dependent adherens junction formation. *Development* **141,** 1282–1291 (2014).
11. Ma, E. Y. & Raible, D. W. Signaling pathways regulating zebrafish lateral line development. *Curr. Biol.* **19,** R381–R386 (2009).
12. Lecaudey, V., Cakan-Akdogan, G., Norton, W. H. J. & Gilmour, D. Dynamic Fgf signaling couples morphogenesis and migration in the zebrafish lateral line primordium. *Development* **135,** 2695–2705 (2008).
13. Nechiporuk, A. & Raible, D. W. FGF-dependent mechanosensory organ patterning in zebrafish. *Science* **320,** 1774–1777 (2008).
14. Aman, A. & Piotrowski, T. Wnt/β-catenin and Fgf signaling control collective cell migration by restricting chemokine receptor expression. *Dev. Cell* **15,** 749–761 (2008).
15. Rohner, N. *et al.* Duplication of fgfr1 permits Fgf signaling to serve as a target for selection during domestication. *Curr. Biol.* **19,** 1642–1647 (2009).
16. Emelyanov, A. & Parinov, S. Mifepristone-inducible LexPR system to drive and control gene expression in transgenic zebrafish. *Dev. Biol.* **320,** 113–121 (2008).
17. Bagnat, M., Cheung, I. D., Mostov, K. E. & Stainier, D. Y. R. Genetic control of single lumen formation in the zebrafish gut. *Nature* **9,** 954–960 (2007).
18. Kolotuev, I., Schwab, Y. & Labouesse, M. A precise and rapid mapping protocol for correlative light and electron microscopy of small invertebrate organisms. *Biol. Cell* **4,** 121–132 (2009).
19. Yu, S. R. *et al.* Fgf8 morphogen gradient forms by a source-sink mechanism with freely diffusing molecules. *Nature* **461,** 533–536 (2009).
20. Raible, F. & Brand, M. Tight transcriptional control of the ETS domain factors Erm and Pea3 by Fgf signaling during early zebrafish development. *Mech. Dev.* **107,** 105–117 (2001).
21. Martin-Belmonte, F. *et al.* Cell-polarity dynamics controls the mechanism of lumen formation in epithelial morphogenesis. *Curr. Biol.* **18,** 507–513 (2008).
22. Kesavan, G. *et al.* Cdc42-mediated tubulogenesis controls cell specification. *Cell* **139,** 791–801 (2009).
23. Hildebrand, J. D. Shroom regulates epithelial cell shape via the apical positioning of an actomyosin network. *J. Cell Sci.* **118,** 5191–5203 (2005).
24. Ernst, S. *et al.* Shroom3 is required downstream of FGF signalling to mediate proneuromast assembly in zebrafish. *Development* **139,** 4571–4581 (2012).

©2014 Macmillan Publishers Limited. All rights reserved

25. Belenkaya, T. Y. *et al. Drosophila* Dpp morphogen movement is independent of dynamin-mediated endocytosis but regulated by the glypican members of heparan sulfate proteoglycans. *Cell* **119,** 231–244 (2004).
26. Donà, E. *et al.* Directional tissue migration through a self-generated chemokine gradient. *Nature* **503,** 285–289 (2013).
27. Bökel, C. & Brand, M. Endocytosis and signaling during development. *Cold Spring Harb. Perspect. Biol.* **6,** a016881 (2014).
28. Bryant, D. M. & Mostov, K. E. From cells to organs: building polarized tissue. *Nature Rev. Mol. Cell Biol.* **9,** 887–901 (2008).
29. Nieto, M. A. Epithelial plasticity: a common theme in embryonic and cancer cells. *Science* **342,** 1234850 (2013).
30. Wang, Y.-C., Khan, Z., Kaschube, M. & Wieschaus, E. F. Differential positioning of adherens junctions is associated with initiation of epithelial folding. *Nature* **484,** 390–393 (2012).

Supplementary Information is available in the online version of the paper.

Acknowledgements We are grateful to J. Ellenberg, S. de Renzis and F. Peri for suggestions and comments on the manuscript, A. Aulehla for advice about timing, and E. Karsenti and the Gilmour laboratory for discussion. We thank M. Brand for advice about FGF tagging, the EMBL Advanced Light Microscopy Facility, in particular Y. Belyaev, for imaging assistance, the European Molecular Biology Laboratory (EMBL) Monoclonal Antibody (MACF) and Protein Expression Facilities for Fgfr1a antibody, K. Miura from the EMBL Centre for Cell and Molecular Imaging for advice with data analysis, E. Dona and T. Gregor for advice with the smFISH protocol, and A. Gruia for fish care. We acknowledge funding from the European Molecular Biology Organization and EMBL Interdisciplinary Postdocs (EIPOD) (to C.R.) and the Deutsche Forschungsgemeinschaft SFB 488 (to D.G.).

Author Contributions D.G. and S.D. designed the study. S.D. performed all experiments, with the exception of CLEM experiments performed with N.S. and Y.S., and antibody-based analysis of the microlumen performed by C.R. S.D. and M.I. developed the data analysis methods with input from P.B. A.K. developed the LexPR inducible gene expression system and C.R. generated the Cxcr4b–RFP line. D.G. and S.D. interpreted the data and wrote the paper with input from all authors.

Author Information Reprints and permissions information is available at www.nature.com/reprints. The authors declare no competing financial interests. Readers are welcome to comment on the online version of the paper. Correspondence and requests for materials should be addressed to D.G. (gilmour@embl.de).

©2014 Macmillan Publishers Limited. All rights reserved

METHODS

Fish handling. Zebrafish (*Danio rerio*) strains were maintained following standard protocols[31]. Embryos were raised in E3 buffer at 26–30 °C. All zebrafish experiments were conducted on embryos younger than 3 d.p.f., under the rules of the European Molecular Biology Laboratory and the guidelines of the European Commission, Directive 2010/63/EU. In all experiments involving chemical treatment, embryos were dechorionated with pronase. Before live imaging and fixation procedures, embryos were anaesthetized with 0.01% tricaine. For *in situ* hybridization and immunostaining experiments, embryos were treated with 0.002% phenylthiourea at 24 hours post-fertilization (h.p.f.) to prevent pigmentation. For live imaging, embryos were mounted in 0.8% low melting agarose in glass-bottom dishes (MatTek or CELLview) and imaged at 28 °C unless otherwise stated. The following mutant and transgenic strains were used: *fgfr1a*^{t3R705H} (ref. 15), *cxcr4b:nls-tdTomato*[26], *cldnb:lynGFP*[32].

Inducible gene expression system and BAC lines. The LexPR/LexOP transactivation system[16] was used to express genes in the lateral line upon addition of the progesterone analogue RU486. Two LexPR 'driver' lines were generated by inserting the cassettes (1) LexPR/polyA/LexOP:lynRFP/SV40polyA/FRT-KanR-FRT or (2) LexPR/SV40poly(A)l/FRT-KanR-FRT into the first exon of the Cxcr4b BAC clone CH211-145M5 by ET recombineering (Gene Bridges). The KanR cassette was subsequently removed with FLP recombinase. To serve as a transgenic marker, the 'crystal eye' cry:CFP/KanR cassette was inserted in the BAC backbone as a transgenic marker. Modified BACs were purified (Large Construct Kit, Qiagen) and injected into one-cell stage embryos to generate transgenic driver lines. The following LexOP 'responder' lines were generated from multisite-gateway clones (Invitrogen) using the Tol2kit[33]: (1) LexOP(p5E)/secGFP(pME)/fgf3(p3E), (2) LexOP (p5E)/secGFP(pME)/polyA(p3E) and (3) LexOP(p5E)/nlsGFP(pME)/polyA(p3E). All clones carry the *cmlc2:eGFP* 'bleeding heart' cassette as a transgenic marker[33]. Fgf3 was tagged by inserting the GFP sequence in between signal peptide (sec) and globular domain of Fgf3, the strategy previously used for Fgf8 (ref. 19). secGFP has the signal peptide of Fgf3 protein fused to GFP. The LexPR system was proved to be non-leaky as there was no detectable target gene expression in the absence of activator RU486. It was also proved to be spatially restricted, showing transactivation only in Cxcr4b-expressing tissues. The dose–response of the inducible LexPR system was evaluated using the transactivation levels of the *lexOP:nlsGFP* responder after treatment for 6 h with 0, 5, 10 and 20 μM RU486. The lateral line primordium was imaged with the same acquisition settings for all samples. The average fluorescence signal from mean projected images was quantified, and these values were first background subtracted (calculated from untreated embryos) and then normalized to [0,1] range by dividing with the maximum signal.

The BAC *fgf3:fgf3–GFP* line was generated by replacing coding sequence of the first exon in Fgf3 BAC (CH211-96B20) with a targeting cassette: secGFP/fgf3/SV40poly(A)/FRT-KanR-FRT. The KanR cassette was subsequently removed with FLP recombinase. The *cry:CFP/ AmpR* 'crystal eye' cassette was inserted into the BAC backbone as a transgenic marker[26]. BAC recombination and purification steps were followed as described[26]. Whole-embryo overview images were generated using a Zeiss Lightsheet Z.1 microscope (×20). The functionality of the BAC line was tested by FGF knockdown rescue experiments, where both Fgf3 and Fgf10a genes were knocked down owing to mutual compensation of the two ligands in lateral line system[12]. Fgf3 (splice site blocker, 5 ng nl^{-1})[34] and Fgf10 (start site blocker, 5 ng nl^{-1})[35] morpholinos were injected into BAC *fgf3:fgf3–GFP*, *cldnb:lynGFP* embryos at the one-cell stage, where half of the embryos were BAC *fgf3:fgf3–GFP* transgene carriers as detected by *cry:eCFP* transgenic marker (Extended Data Fig. 6). The *cxcr4b:cxcr4b-tagRFP* line was generated by inserting TagRFP cassette into the Cxcr4b BAC (CH211-145M5) as described[26].

Chemical treatments. SU5402 (Calbiochem) was used for inhibition of Fgfr1 kinase activity. Eight embryos per 2 ml of E3 buffer were used as standard treatment density. For organ deposition experiments, embryos were treated with 0.5 and 1 μM SU5402 in 0.1% dimethylsulphoxide (DMSO) starting at 24 h.p.f.; controls were treated with 0.1% DMSO alone. Time-lapse imaging was started at 4–6 h after treatment, when the first organ was about to be deposited. Drug efficacy was observed to decrease over time-lapse imaging owing to light sensitivity of SU5402. Therefore, organ spacing was quantified as 2 d.p.f. measurements on embryos that were kept in the dark.

RU486 (Sigma) was used to transactivate LexPR/LexOP driven gene expression. For organ deposition experiments, *cxcr4b:lexPR, lexOP:fgf3–GFP* embryos were treated with 5, 10 and 20 μM RU486 starting at 24 h.p.f. Time-lapse imaging was started at 4–6 h after treatment. As a control group, *cxcr4b:LexPR* transgenics without *lexOP:fgf3–GFP* were treated with 10 μM RU486.

Brefeldin A (BFA, Sigma) was used to visualize localization of Fgf3–GFP in the absence of secretion. Embryos were first treated with 15 μM RU486 for 4–6 h to express Fgf3–GFP and then treated with 14 μM BFA for 30 min to block secretion.

Immunofluorescence and colorimetric *in situ* hybridization. Monoclonal anti-Fgfr1a antibody was generated using the following peptide, corresponding to 140–360 amino acids of Fgfr1a protein as an antigen: 'KLSNDQNLPMAPVWAQP DKMEKKLHAVPASKTVKFRCQANGNPTPTLKWLKNGKEFKRDQRIGGFK VREHMWTIIMESVVPSDRGNYTCLVENRHGSINHTYQLDVVERSPHRPILQ AGLPANRTAVVGSDVEFECKVFSDPQPHIQWLKHIEVNGSRYGPDGLPYV RALKTAGVNTTDKEMEVLQIRNVSLEDAGEYTCLAGNSIGHSHHSAWLTV YKA'. For whole mount antibody staining, embryos were fixed with pre-cooled 85% methanol, 15% acetic acid for 3 min at −20 °C and rehydrated with methanol series 75, 50, 25%, 3 min each at room temperature (~23 °C). Blocking was done with blocking buffer (1× PBS, 1% DMSO, 2% NCS, 1% BSA, 0.1% Tween) for 4 h at room temperature. Embryos were then incubated with primary antibody (1:50 in blocking buffer) for 20 h at 4 °C. Embryos were washed with blocking buffer four times for 30 min at room temperature and incubated with Alexa 488-anti-mouse antibody (1:500 in blocking buffer) for 2.5 h at room temperature. Embryos were then washed with blocking buffer four times for 30 min and mounted in 1% LM agarose. Samples were imaged using an Ultraview VoX spinning disk confocal microscope with a ×63 Zeiss water objective (1.2 numerical aperture).

ZO1 antibody staining (anti-ZO1 primary antibody, Alexa-568-coupled anti-mouse secondary antibody) and *pea3 and fgf3 in situ* hybridization (DIG probes, anti-DIG alkaline phosphatase coupled antibody, NBT/BCIP substrate at 30 °C) were performed as described previously[12].

Analysis of migration and organ patterning. Embryos were imaged with PE Ultraview ERS and PE Ultraview VoX spinning disk microscopes using Zeiss ×5, ×10, ×20 air objectives. Multi-position time-lapse images were acquired from 10 to 30 min intervals and a computational pipeline to analyse migration and organ patterning was established. First, images of individual embryos were stitched automatically by a macro using Grid stitching tool in FIJI[36]. To analyse time-lapse movies, kymographs (*x–t* graphs) were generated using FIJI. For each embryo, a segmented line region of interest (ROI) was drawn along the migration path of the primordium with a thickness that covered the lateral line primordium. The image beneath the line ROI was re-sliced (from *xy–t* to *xt–y*) and maximum projected. This way maximum signal intensity along the width of the tissue was represented in the kymograph for each time point. Images were then saved as text images to be automatically processed with an R script. Organ positions were determined with a peak detection algorithm implemented in R package 'Peaks'[37]. To map the trajectory of each organ, kymographs were sequentially processed in reverse order from the last time frame to the first. A wide range of parameters (threshold from 10 to 50 in increments of 10, and sigma from 3 to 9 in increments of 3) was used for peak detection, since the signal intensity profiles change over time. We manually checked whether the peaks identified at the last frame referred to an organ or not; only those that did refer were retained as starting points for tracking. For the remaining time points, the hypothetical position of each organ was initially estimated on the basis of the average displacement of the last three time points, then the closest position was sequentially linked to the trajectory between consecutive time points (Supplementary Video 2). Velocity and acceleration profiles of organs were generated from the migration trajectories using local polynomial fitting and its derivatives (KernSmooth package in R)[38]. Organ deposition was defined as the time point where acceleration of the individual organ unit was minimum. We defined three potential parameters that influence organ patterning: (1) embryo growth, (2) primordium migration velocity and (3) organ deposition timing. As higher growth rate between two organ depositions could hypothetically result in increased spacing, we evaluated the effect of embryonic growth by generating trajectories of manually segmented myotome borders, as embryonic landmarks, from kymographs generated using transmission light images. Next, myotome trajectories were subtracted from lateral line organ trajectories using the closest myotome for each organ and each time point. Finally, 'growth-subtracted' organ positions were calculated, revealing that in the absence of embryonic growth, organ spacing would decrease overall without much effect on relative spacing. We next evaluated the effect of primordium migration velocity and organ deposition timing on organ spacing. If primordium velocity was higher between two organ depositions, or the following organ was deposited later, the spacing between these organs would increase. Correlation of these two parameters with spacing revealed that organ deposition timing is the main determinant of the global organ patterning in WT embryos.

CLEM. SecGFP, nls-tdTomato-expressing embryos were live imaged (sagittal plane) with a confocal microscope using a ×10 objective for whole-embryo overviews, to aid tissue sectioning, and ×63 objective for high-resolution imaging of lateral line organs, to aid three-dimensional CLEM image construction. After live imaging, embryos were removed from agarose, anaesthetized and tails were removed by cutting after the yolk extension. Bodies were immediately fixed with 2.5% glutaraldehyde and 4% paraformaldehyde in 0.1 M PHEM buffer for 14 min in a Pelco BioWave microwave containing ColdSpot (100 W cycling intervals of 2 min on and off under vacuum). Further processing was performed as described[18], although using 0.1 M

©2014 Macmillan Publishers Limited. All rights reserved

PHEM buffer instead of cacodylate buffer. Samples were flat embedded between aclar sheets and polymerized at 60 °C for 48 h. Lateral line organs were targeted for further processing by overlaying whole-embryo overviews of live imaging and images of fixed-embedded samples (CLEM targeting approach as described elsewhere[18]). Melanocytes were used as landmarks to correlate the two data sets and then as guides to laser etch the block surface with an Olympus Cell^R with UV Cutting. Serial sections were cut 70 nm thick along the dorsoventral axis of the embryo (transverse plane) and placed on a copper palladium slot grid, coated with 1% Formvar (Serva).

Electron microscope imaging was performed on a CM120 Phillips electron microscope. Serial images were aligned with Adobe Photoshop and structures of interest were tracked manually in 3dmod[39]. Electron and fluorescence microscopy images were further processed in Imaris 7.6.4 (Bitplane) for three-dimensional image handling. Nucleus positions of the target organs in electron microscopy images (dark grey) and fluorescence images (nls-tdTomato) were compared using the oblique slicer tool in Imaris to identify the correct transversal sectioning angle. Fluorescence images were then re-sliced using the identified angle. Shrinkage of electron microscope samples was calculated by comparing three-dimensional tissue size in electron microscope images and fluorescence images, then fluorescence images were resized accordingly. The central slice of electron microscope images and the corresponding fluorescence image were overlaid as shown in Extended Data Fig. 4m. A three-dimensional CLEM image construction of an organ centre with segmented structures is displayed in Supplementary Video 7.

FRAP and FLIP. Photo-bleaching experiments were performed using an Ultraview VoX spinning disk microscope equipped with a photokinesis unit and Zeiss ×63 water objective. Position accuracy of the laser pulse was calibrated using green fluorescent slides before each experiment. Experiments were performed on middle confocal planes of secGFP and Fgf3–GFP pools. In FLIP experiments, five pre-bleach images were acquired (0.018 s per frame), then a small region (spot ROI with 0.73 μm diameter) was repetitively bleached (45 time points) and the sample imaged in between (0.3 s per frame). Images were analysed by measuring mean intensity over time of (1) bleached region, (2) total pool, (3) background and (4) multiple other regions within the pool. In FRAP experiments, five pre-bleach images were acquired (30 ms per frame), then a strip ROI on the edge of the pool was bleached once and post-bleach images were acquired (45 time points, 30 ms per frame). Images were analysed by measuring mean intensity over time of (1) bleached region, (2) total pool and (3) background. Next, the measurements were uploaded to easyFRAP to calculate half-time of recovery with full-scale normalization and double term fitting[40]. Small spot ROI bleaching in the centre of the pool could not be used for FRAP experiments as the redistribution of the protein was too fast to catch recovery curves. This fast distribution could also be seen by the FLIP experiments with a spot ROI bleaching.

Secretory pathway analysis. *In vitro* synthesized messenger RNAs (mRNAs) (100 ng μl^{-1}) encoding GM130-tdTomato and KDEL peptide fused to mKate2 were injected into one-cell stage embryos to label the Golgi apparatus and endoplasmic reticulum, respectively. GM130-tdTomato signal was segmented in three-dimensions and used as a landmark for density profile plotting of secGFP and Fgf3–GFP intensities within each cell.

Single-cell overexpression experiments. Fgf3–GFP mis-expressing cell clones were generated by cell transplantation, following established protocols. Donor cells from *cxcr4b:lexPR, lexOP:lynRFP, lexOP:Fgf3–GFP, cxcr4b:nls-tdTomato* transgenic embryos were transplanted into *cldnb::lynGFP* transgenic embryos, allowing Fgf3-expressing clones to be marked with nuclear tdTomato in membrane GFP-labelled hosts. *Cxcr4b:nls-tdTomato* cells were transplanted into *cldnb::lynGFP* embryos as controls. Time-lapse imaging was performed and the effect of FGF mis-expression was analysed by comparing migration behaviour of organs with and without clones. Primordium velocity, organ spacing and organ deposition timing between two consecutive depositions were quantified. To correct for intrinsic variation, which is high among WT organ intervals (see Fig. 1a and Extended Data Fig. 1), calculated values for each interval were normalized to the mean of the corresponding interval from controls.

To generate Fgf3–GFP-overexpressing clones by mosaic expression, the *lexOP:Fgf3–GFP* plasmid was injected into *cxcr4b:lexPR, cxcr4b:nls-tdTomato* transgenic embryos at the one-cell stage. The next day, Fgf3–GFP expression was observed in randomly positioned cells. Overview images of the lateral line were acquired at 2 d.p.f. to analyse organ patterning; water injected embryos were used as controls. Organ spacing in Fgf3–GFP microlumina-positive and -negative organs was analysed by normalizing each interval to control embryos as described for the transplantation experiment above.

smFISH. smFISH probes (Custom Stellaris FISH probes, Biosearch Technologies) were designed to target *pea3* mRNA (ENSDART00000013033). Forty-eight sequence-specific oligonucleotides (listed below) were conjugated to the fluorophores Cal Fluor 590 (red) and Quasar 670 (far red). Embryos were fixed and permeabilized following standard zebrafish *in situ* hybridization protocols. smFISH was performed following the procotol of ref. 41, with the exception that 5× SSC replaced 2× SSC in the hybridization buffer, and embryos were stained with DAPI for 15 min at 30 °C after probe removal. Embryos hybridized with Cal Fuor 590 conjugated probes were mounted in Aquamount (Polysciences). Embryos hybridized with Quasar 670 conjugated probes were mounted in GLOX buffer (0.4% glucose, 10 mM TrisHCl (pH 8), 2× SSC, 0.16 mg ml^{-1} glucose oxidase, 0.02 mg ml^{-1} catalase in ddH20) and imaged immediately to prevent bleaching. Imaging was performed using a ×100 Zeiss oil objective (1.4 numerical aperture) and a PE Ultraview VoX spinning disk microscope with 0.07 μm pixel size and 0.2 μm *z* steps. For Cal Fluor 590 conjugated probes, 561 nm excitation, 620(W60) emission, and for Quasar 670 conjugated probes, 640 nm excitation, 705(W90) emission, were used.

smFISH images were analysed in Imaris 7.6.4 (Bitplane). First, a volume of interest (surface object) was defined by manually tracking borders at multiple *z* slices considering membrane and nucleus labelling ('contour surface' tool). Nuclei were counted using the spot segmentation tool with 2.5 μm estimated diameter, then identified nucleus points were manually corrected for missing or fused selections. The RNA signal was counted using the spot segmentation tool with region growing, local contrast algorithms and 0.4 μm estimated diameter. Identified spots were filtered to have at least 0.4 μm diameter in the *z* dimension (Supplementary Video 9). Positions of nuclei and RNA spots were exported from Imaris to be processed further in R. Transcript count per cell was calculated by simply dividing the number of identified transcripts by the number of nuclei.

Transcript profiles along the posterior–anterior axis of the primordium were generated by fitting a line (the first principal component) to the nucleus positions along the long axis of the primordium. Then, segmented transcript and nuclei positions were projected on this line and their ratio along the primordium was plotted with 10 μm sliding window. Transcript distributions of a mosaic embryo organ were represented by assigning the transcripts to the closest nucleus position in two dimensions.

To test the validity of the *pea3* smFISH protocol to be used as FGF signalling read-out, embryos were treated with 4 μM SU5402 FGF inhibitor and 15 μM FGF inducer for 6 h. *Pea3* smFISH protocol was applied on four WT, four FGF-induced and four Fgfr-inhibited primordia (an average of 150, 143 and 195 cells per primordium respectively), and transcript counts per cell were plotted.

The relation between luminal FGF levels and *pea3* transcription response was tested by inducing *lexOP:Fgf3–GFP* expression with 5 μM and 20 μM inducer for 6 h to generate a wide range of expression levels. Organ 1 of each embryo was imaged using an Ultraview VoX spinning disk confocal microscope and a ×63 Zeiss water objective (1.2 numerical aperture) with the same imaging settings. Embryos were then fixed and processed individually for smFISH protocol to compare their luminal Fgf3–GFP intensity with *pea3* transcript counts.

Pea3 smFISH oligonucleotides: 1, AAGGAAGACGGACAGAGGCA; 2, CTGTGTTTTAATGAGCTCCA; 3, CTTAACCGTTTGTGGTCATT; 4, CCATCCATCTTATAATCCAT; 5, AGTATAAGGCACTTGCTGGT; 6, ATTTCCTTGCGACCTATTAG; 7, TCAACAGTCTATTTAGGGGC; 8, ATGTATTTCCTTTTTGTCGC; 9, AAGAGGTCTTCAGATTCCTG; 10, CCTGAAGTTGGCTTAAATCC; 11, GGAACTTGAGCTTCGGTGAG; 12, AACAAACTGCTCATCGCTGT; 13, CACTGAGTTCTCTGAGTGAA; 14, TTCTTAATCTTCACAGGCGG; 15, TAGCTGAAGCTTTGCTTGTG; 16, TCATAGGCACTGGCGTAAAG; 17, CTGGACATGAGCTCTTAGAT; 18, TTGGGGGAATAATGCTGCAT; 19, TGAGGGTGGATTCATATACC; 20, CGGAAGGGAACCTGGAACTG; 21, AGAGTGTTGCCGATGGAAAC; 22, TGCTGAGGAGGATAAGGCAA; 23, CCATGTACTCCTGCTTAAAG; 24, TCCTGTTTGACCATCATATG; 25, CAGGTTCGTAAGTGTAGTCG; 26, TGTGATGGTACATGGATGGG; 27, AAACATGTAGCCTTCACTGT; 28, TGGCACAACACGGGAATCAT; 29, TCACCTCACCTTCAAATTTC; 30, ACCTTCACGAAACACACTGC; 31, TAGTTGAAGTGAGCCACGAC; 32, GAAGGGCAACCAAGAACTGC; 33, ATGCGATGAAGTGGGCATTG; 34, ATGAGTTTGAATTCCATGCC; 35, TTGTCATAGTTCATGGCTGG; 36, GTAACGCAAAGAGCGACTCA; 37, TTTTGCATAATTCCCTTCTC; 38, AGGTTATCAAAGCTTCTGGC; 39, CGCTGATTGTCGGGAAAAGC; 40, GTTGACGTAGCGCTCAAATT; 41, AAGAAACTCCCTCATCGAGG; 42, TACATGTAGCCTTTGGAGTA; 43, AAAGGAGAATGTCGGTGGCA; 44, GTGGTAAACTGGGATGGGAA; 45, ATACAAGAGGATGGGGTGGG; 46, GAATGCAGAGTCCCTAATGA; 47, AGATAGGCCTCAGAAGTGAG; 48, GCAATCTCTTGAACCACAGT.

Shroom3 knockdown. Shroom3a was knocked down using a previously published morpholino (5′-CCTAATAAATTGTTACCTGACTAAC-3′, Gene Tools, 4.2 pmol per embryo)[24]. Consistent with the published report, the effect of knockdown on apical constriction was observed to be transient. To measure Pea3 levels in the absence of microluminal trapping, only primordia without visible apical constriction were processed further for smFISH analysis.

Laser micropuncture. Micropuncture experiments were performed with a Zeiss LSM 780 NLO 2-Photon microscope with a Zeiss ×63 water objective (1.2 numerical aperture). SecGFP and Fgf3–GFP pools were focused, and a laser (two-photon

©2014 Macmillan Publishers Limited. All rights reserved

960 nm laser) pulse was applied on different regions of the pool. A minimal pulse size (ROI diameter) of 0.43 μm was selected to allow lumen opening with undetectable damage to participating cells. Targeting single pulses at these settings to the middle section of the pool resulted in a one-time reduction in total fluorescence signal, which we term FLIP. Targeting identical pulses to the microluminal lattice caused micropuncture, as revealed by a characteristic decay caused by leaking of the GFP pool through time. For mean fluorescence intensity plots, five time points before the pulse and 20 or more time points after the pulse were acquired, at a rate of 1 s per frame. To perform analysis of target gene response (*pea3*) to micropuncture, embryos were treated sequentially over a 30 min session. After the laser surgery, embryos were incubated for 30 min, allowing each organ 30–60 min response time after micropuncture before fixation for smFISH analysis. As there was high intrinsic variability of transactivation using the LexPR system (Extended Data Fig. 2), this resulted in variability in target gene response (Fig. 3). Therefore, to allow direct comparison of transcript counts, values were normalized to the first organ of each embryo that was left unperturbed. In control embryos, there is a clear trend where more mature organs have higher expression of *pea3*, presumably because of longer or higher exposure to microluminal FGF. Thus, unperturbed first and third organs provided internal controls. Laser micropuncture causes the second organ to have significantly lower transcript counts than the less mature third organ, a result never observed in non-micropunctured controls.

The effect of micropuncture on FGF signalling was further investigated by performing smFISH protocol immediately after ($t < 2$ min), 1 h after and 4 h after micropuncture. The transcript count per cell of the punctured organ 2 was normalized internally to the unperturbed organ 3.

To test the effect of microluminal FGF loss after micropuncture on collective cell behaviour, different organs before their depositions were micropunctured and the end-point spacing of the corresponding organ was compared with the unperturbed siblings. For Fgf3–GFP overexpression experiments, embryos were induced with 20 μM inducer at 24 h.p.f. At 28 h.p.f., embryos with similar Fgf3–GFP overexpression levels were pre-selected to eliminate sample variability due to drug induction. Organ 2 or 3 was punctured while organ 1 or organ 2 was being deposited, respectively. For secGFP expression experiments, the same strategy was followed without pre-screening for expression levels as secGFP is a neutral marker to visualize intact luminal space.

Statistical analysis. All statistical analysis used R. A non-parametric Wilcoxon rank-sum test (two sided) was used to compare two groups. Sample sizes (n) and P values (P) for each experiment are indicated in figure legends and exact P values are listed below. The statistical dependence between two variables was assessed with Spearman's rank correlation coefficient.

In experiments of organ patterning, more than 50 samples were acquired and automatically analysed to ensure adequate statistical power. For the experiments of transplantation, micropuncture and smFISH analysis, the number of samples was mainly constrained by the complexity of the experimental procedure, data acquisition and analysis capacity. In each experiment, data were analysed after the completion of data collection. To prevent selection bias, samples of stage and genotype matched pools were randomly divided into experimental groups. Additionally, data were analysed automatically where possible to avoid subjective assessments (for example, analysis of organ patterning and smFISH transcript counts).

Boxplots are standard box and whisker plots showing median and interquartile range. For all the experiments, original data points were displayed as scatter plots on top of boxplots using the beeswarm package[42], allowing direct examination of the variance and distribution of the samples.

***P* values and sample sizes.** Fig. 1b: Spearman $r^2 = 0.77$, $N = 82$, $n = 260$. Fig. 1c: $n_{ctrl} = 82, n_{05} = 114, n_1 = 104, P_{ctrl\text{-}05} = 3.94 \times 10^{-24}, P_{05\text{-}1} = 6.99 \times 10^{-29}$. Fig. 1d: $n_{ctrl} = 64, n_5 = 57, n_{10} = 65, n_{20} = 58, P_{ctrl\text{-}5} = 3.87 \times 10^{-5}, P_{5–10} = 3.71 \times 10^{-4}, P_{10–20} = 1.36 \times 10^{-5}$. Fig. 3d: $N_{ctrl} = 38$, $N_{mosaic} = 114$, $n_{ctrl} = 141$, $n_{neg} = 170$, $n_{pos} = 240, P_{ctrl–neg} = 0.9203, P_{ctrl–pos} = 1.29003 \times 10^{-38}, P_{neg–pos} = 3.80489 \times 10^{-32}$. Fig. 3e: $N_{WT} = 4$, $N_{inducer} = 4$, $N_{inhibitor} = 4$, $P_{WT\text{-}inducer} = 0.0285$, $P_{WT\text{-}inhibitor} = 0.0285$. Fig. 3f: Spearman $r^2 = 0.85$, $N = 18$. Fig. 3g: $n_{ctrl} = 4$, $n_{neg} = 9$, $n_{pos} = 7$, $P_{ctrl–neg} = 0.6042$, $P_{neg–pos} = 0.0001748$. Fig. 4b: $N_{WT} = 6$, $N_{shroomMO} = 6$, $P = 0.00216$. Fig. 4e: $N_{ctrl} = 6$, $N_{puncture} = 16$, $P = 0.0003217$. Fig. 4f: second organ: $N_{ctrl} = 16$, $N_{puncture} = 23$, $P = 1.443 \times 10^{-8}$; third organ: $N_{ctrl} = 7$, $N_{puncture} = 7$, $P = 0.002331$. Fig. 4g: $N_{closed} = 6$, $N_{open} = 6$, $P = 0.002165$. Extended Data Fig. 1: Spearman $N = 82$, $n = 260$, $x–t\ r^2 = 0.77$, $x–v\ r^2 = 0.25$, $v–t\ r^2 = -0.07$. Extended Data Fig. 2b: $N_5 = 44$, $N_{10} = 34$, $N_{20} = 32$, $P_{5–10} = 2.53 \times 10^{-8}$, $P_{10–20} = 4.03 \times 10^{-8}$. Extended Data Fig. 2d: $n_{ctrl} = 78, n05 = 71, n1 = 74, P_{ctrl\text{-}05} = 6.22 \times 10^{-14}, P_{05\text{-}1} = 7.26 \times 10^{-4}$. Extended Data Fig. 2e: $n_{ctrl} = 109, n_5 = 112, n_{10} = 119, n_{20} = 137$, $P_{ctrl\text{-}5} = 1.33 \times 10^{-10}$, $P_{5–10} = 7.06 \times 10^{-4}$, $P_{10–20} = 2.46 \times 10^{-4}$. Extended Data Fig. 2f: spacing: $N_{ctrl} = 49$, $N_{mut} = 39$ $P = 7.69 \times 10^{-14}$; timing: $N_{ctrl} = 31$, $N_{mut} = 28$, $P = 4.64 \times 10^{-11}$. Extended Data Fig. 6d: $N_{WT} = 9$, $N_{rescue} = 13$, $N_{FGFmo} = 14$, $P_{WT\text{-}rescue} = 0.09$, $P_{rescue\text{-}FGFmo} = 1.751 \times 10^{-6}$. Extended Data Fig. 7b: $N_{control} = 7$, $N_{transplants} = 8$, $n_{control} = 25$, $n_{neg} = 17$, $n_{pos} = 13$; spacing: $P_{ctrl–neg} = 0.24$, $P_{ctrl–pos} = 1.43 \times 10^{-5}$, $P_{neg–pos} = 4.40 \times 10^{-5}$; timing: $P_{ctrl–neg} = 0.07$, $P_{ctrl–pos} = 1.23 \times 10^{-6}$, $P_{neg–pos} = 4.09 \times 10^{-5}$. Extended Data Fig. 9d: $N_{0\,h\ puncture} = 6$, $N_{0\,h\ control} = 5$, $N_{1\,h\ puncture} = 6$, $N_{1\,h\ control} = 5$, $N_{4\,h\ puncture} = 6$, $N_{4\,h\ control} = 5$, $P_{0\,h} = 0.7922, P_{1\,h} = 0.0043, P_{4\,h} = 0.4286$. Extended Data Fig. 9e: $N_{ctrl\ second\ organ} = 22, N_{puncture\ second\ organ} = 23, N_{ctrl\ third\ organ} = 8, N_{puncture\ third\ organ} = 9, P_{second\ organ} = 6.928 \times 10^{-6}$, $P_{third\ organ} = 0.0061$.

31. Westerfield, M. *The Zebrafish Book* 5th edn (Univ. Oregon Press, 2007).
32. Haas, P. & Gilmour, D. Chemokine signaling mediates self-organizing tissue migration in the zebrafish lateral line. *Dev. Cell* **10,** 673–680 (2006).
33. Kwan, K. M. *et al.* The Tol2kit: a multisite gateway-based construction kit for Tol2 transposon transgenesis constructs. *Dev. Dyn.* **236,** 3088–3099 (2007).
34. Kwon, H. J. & Riley, B. B. Mesendodermal signals required for otic induction: Bmp-antagonists cooperate with Fgf and can facilitate formation of ectopic otic tissue. *Dev. Dyn.* **238,** 1582–1594 (2009).
35. Norton, W. H. J., Ledin, J., Grandel, H. & Neumann, C. J. HSPG synthesis by zebrafish Ext2 and Extl3 is required for Fgf10 signalling during limb development. *Development* **132,** 4963–4973 (2005).
36. Preibisch, S., Saalfeld, S. & Tomancak, P. Globally optimal stitching of tiled 3D microscopic image acquisitions. *Bioinformatics* **1,** 1463–1465 (2009).
37. Morhac, M. Peaks: Peaks. R package v.0.2. (http://cran.r-project.org/web/packages/Peaks/Peaks.pdf, 2012).
38. Wand, M. KernSmooth: functions for kernel smoothing for Wand & Jones (1995). R package v.2.23-10. (http://cran.r-project.org/web/packages/KernSmooth/KernSmooth.pdf, 2011).
39. Kremer, J. R., Mastronarde, D. N. & McIntosh, J. R. Computer visualization of three-dimensional image data using IMOD. *J. Struct. Biol.* **116,** 71–76 (1996).
40. Rapsomaniki, M. A. *et al.* easyFRAP: an interactive, easy-to-use tool for qualitative and quantitative analysis of FRAP data. *Bioinformatics* **1,** 1800–1801 (2012).
41. Raj, A., van den Bogaard, P., Rifkin, S. A., van Oudenaarden, A. & Tyagi, S. Imaging individual mRNA molecules using multiple singly labeled probes. *Nature Methods* **5,** 877–879 (2008).
42. Eklund, A. beeswarm: The bee swarm plot, an alternative to stripchart. R package v.0.1.6 (http://cran.r-project.org/web/packages/beeswarm/beeswarm.pdf. 2013).

©2014 **Macmillan Publishers Limited. All rights reserved**

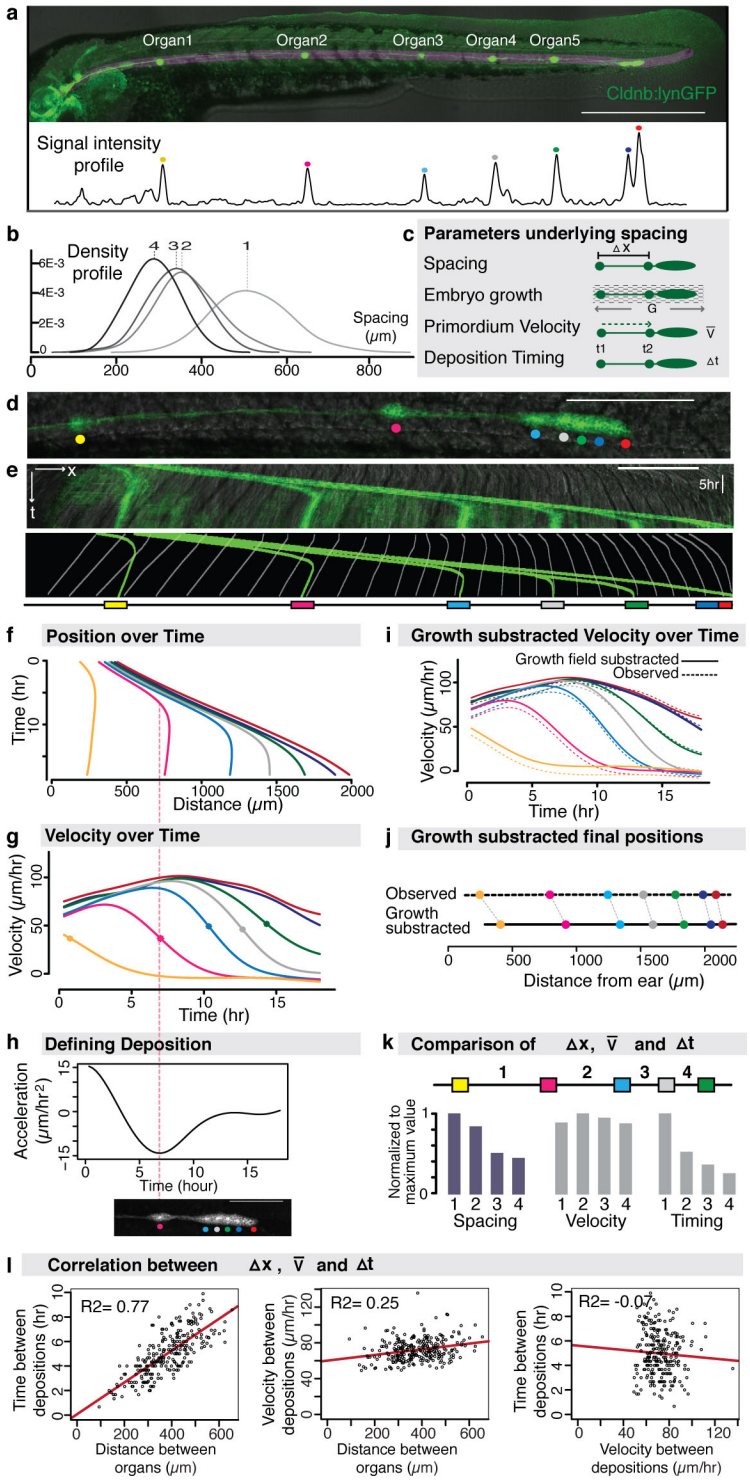

Extended Data Figure 1 | Quantitative analysis of lateral line organ deposition. **a**, Posterior lateral line organs at 2 d.p.f. (*cldnb:lynGFP*). Organ positions were identified from intensity profiles using peakFinder_R. **b**, Density profile of distance between consecutive organ positions (first, second, third and fourth spacing interval; see Fig. 1a). **c**, List of potential parameters affecting organ spacing. **d**, *cldnb:lynGFP* and brightfield overlay image. Spheres indicate colour code representing individual organs used in further analysis. **e**, Upper panel, kymograph (*x*–*t* graph) from a 17.6 h time-lapse movie, where the *y* axis represents time and the *x* axis represents distance. Lower panel, segmented kymograph of primordium migration (green) and myotome growth (dashed lines) through time. **f**, **g**, Calculated position (**f**) and velocity (**g**) of each organ through time. Asterisk shows the time point when organ disengages from the migrating collective. **h**, Second organ acceleration through time. Organ deposition is defined as the time where acceleration is minimum. **i**, Growth-effect-subtracted velocity of each organ through time (solid lines) versus observed velocities (dashed line). **j**, Reconstruction of organ positions from growth-subtracted velocities. **k**, Comparing spacing, average velocity and time between consecutive depositions for first, second, third and fourth interval (normalized to maximum). **l**, Correlation of time, distance and average velocities between consecutive depositions. Statistics: Spearman $N = 82$, $n = 260$, x–t $r^2 = 0.77$, x–v $r^2 = 0.25$, v–t $r^2 = -0.07$. Scale bars, 500 μm (**a**), 200 μm, 5 h (**d**, **e**).

©2014 Macmillan Publishers Limited. All rights reserved

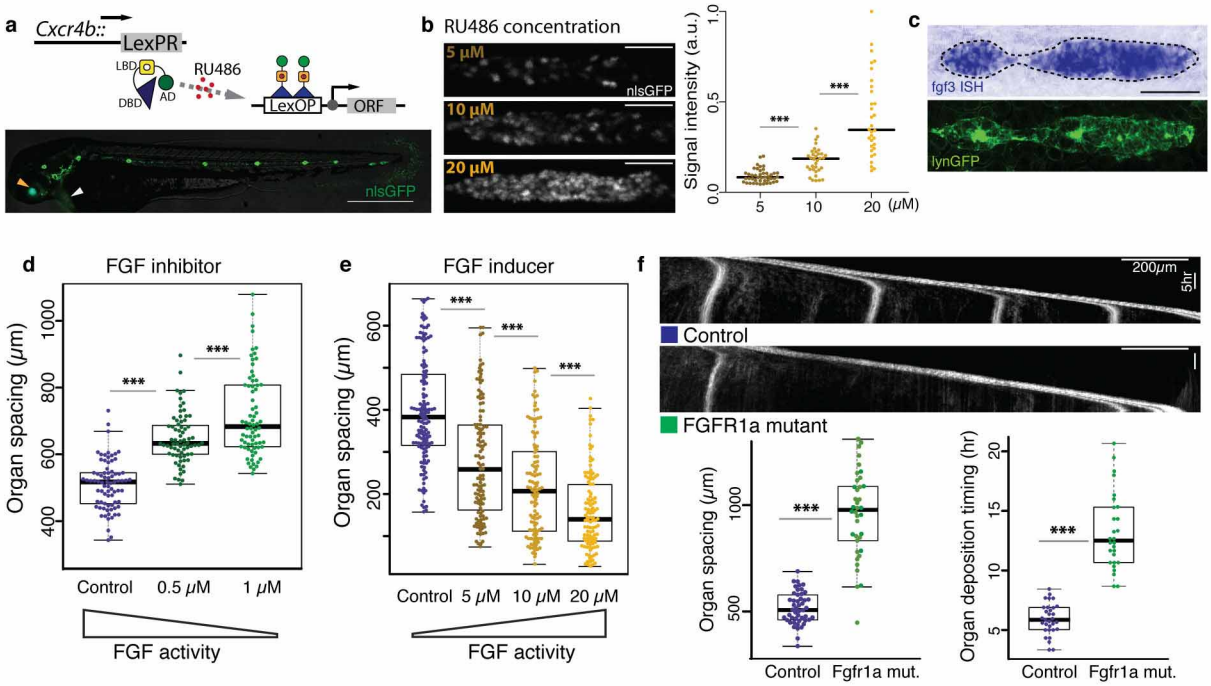

Extended Data Figure 2 | 'Tunable' drug-inducible gene expression with LexPR and quantification of dose-dependent response to FGF signalling. **a**, Schema shows transactivator LexPR expressed under the control of CXCR4b promoter (*Cxcr4b:LexPR)* driving expression of LexOP-coupled coding sequences upon addition of inducer RU486 (above). Image of *cxcr4b:LexPR*-driven expression of *lexOP:nlsGFP* showing spatially restricted expression upon RU486 treatment. Scale bar, 500 μm (*cry:eCFP* 'crystal eye' marker: orange arrow; *clmc2:GFP* 'bleeding heart' marker: white arrow). **b**, Mean fluorescence intensity projection of *Cxcr4b:LexPR, LexOP:nlsGFP* primordium treated with 5 ($n = 44$), 10 ($n = 34$) and 20 μM ($n = 32$) RU486. Scale bar, 50 μm. Plot shows quantification of signal intensity after 4 h of RU486 induction ($P_{5-10} = 2.53 \times 10^{-8}$, $P_{10-20} = 4.03 \times 10^{-8}$). **c**, Colorimetric *in situ* hybridization of *fgf3* mRNA in *Cxcr4b:LexPR, LexOP:Fgf3–GFP* showing uniform expression. Scale bar, 50 μm. **d**, **e**, Organ spacing in FGF inhibitor- and inducer-treated embryos at 2 d.p.f. **d**, Quantification of organ spacing ($n = 78$, 71, 74, $P_{ctrl-05} = 6.22 \times 10^{-14}$, $P_{05-1} = 7.26 \times 10^{-4}$) in SU5402-treated samples. **e**, Quantification of organ spacing ($n = 109$, 112, 119, 137, $P_{ctrl-5} = 1.33 \times 10^{-10}$, $P_{5-10} = 7.06 \times 10^{-4}$, $P_{10-20} = 2.46 \times 10^{-4}$) in RU486-treated samples. **f**, Organ depositions in WT and homozygous *fgfr1a*^{t3R705H} mutants shown by kymographs of 21 h time-lapse movies. Quantification of spacing ($n = 49$, 39, $P = 7.69 \times 10^{-14}$) and deposition timing ($n = 31$, 28, $P = 4.64 \times 10^{-11}$) between organs (first interval). Scale bar, 200 μm, 5 h.

©2014 Macmillan Publishers Limited. All rights reserved

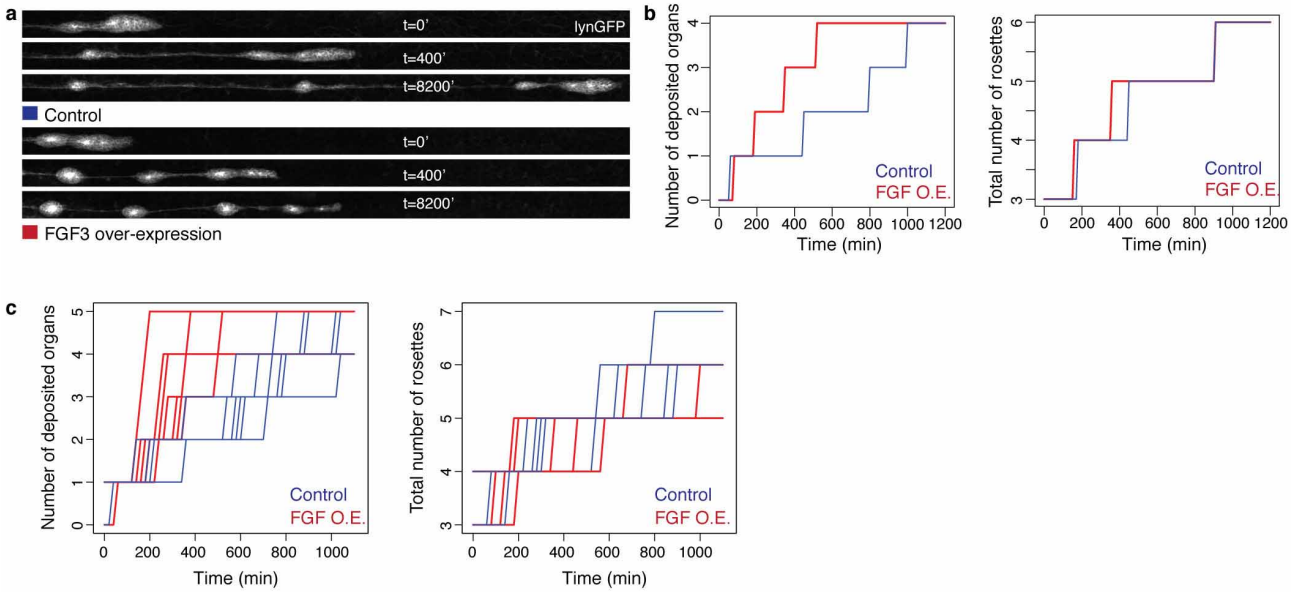

Extended Data Figure 3 | Organ deposition and rosette formation rate upon Fgf3–GFP overexpression. **a**, *cldnb:lynGFP* embryos showing comparison of organ deposition and rosette formation rate upon *lexOP:fgf3–GFP* overexpression. **b**, **c**, Comparisons of total number of organs deposited (left) and total number of organ progenitor rosettes assembled (right) through time in control (blue) and *lexOP:fgf3–GFP* (red) embryos. Only organ deposition timing shows a clear difference between these conditions. **c**, Plots showing multiple examples of data in **b** ($n = 7, 7$).

©2014 Macmillan Publishers Limited. All rights reserved

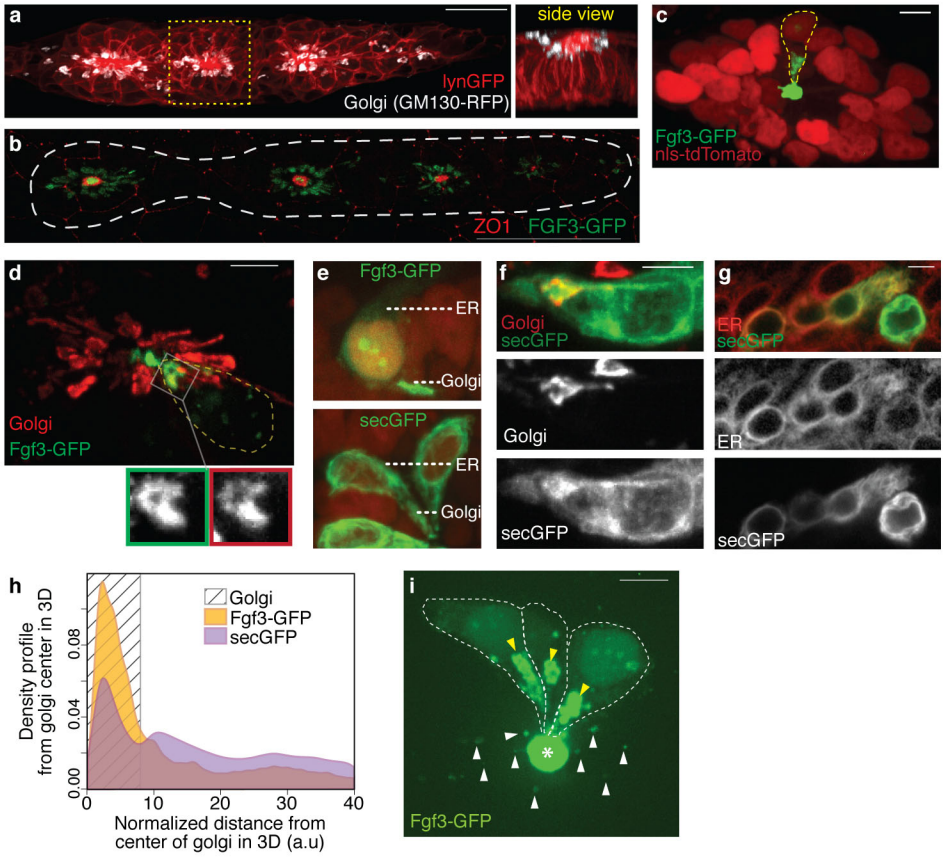

Extended Data Figure 4 | SecGFP and Fgf3–GFP localization in apically polarized secretory path. **a**, Golgi, labelled by GM130-tdTomato (white) mRNA injection, are localized apically around rosette centres in lateral line primordium (*cldnb:lynGFP*, red). Scale bar, 20 µm. **b**, Maximum projection of apical optical sections of a transgenic *lexOP:fgf3–GFP* primordium, counterstained for ZO1, shows intracellular Fgf3–GFP signal around rosette centres in addition to luminal signal. Scale bar, 50 µm. **c**, Single cell expressing Fgf3–GFP feeds the central microlumen through apical secretion (expressing cell indicated with yellow dashed line). Scale bar, 5 µm. **d**, Mosaic primordium showing apically localized intracellular Fgf3–GFP signal co-localizes with Golgi marker GM130-tdTomato. Scale bar, 5 µm. **e**, Intracellular Fgf3–GFP and secGFP localization at secretory path. **f**, Golgi (GM130-tdTomato) co-labelling with secGFP. Scale bar, 5 µm. **g**, Endoplasmic reticulum (mKate2-KDEL) co-labelling with secGFP. Scale bar, 5 µm. **h**, Signal distribution of secGFP and Fgf3–GFP in three dimensions within the expressing cell where Golgi was taken as a central point. Comparison of Fgf3–GFP and secGFP density profiles suggests that Fgf3–GFP is more pronounced in Golgi ($n_{secGFP} = 5$, $n_{Fgf3–GFP} = 4$). **i**, Imaging of Fgf3–GFP-expressing clones (white dashed lines) with high sensitivity reveals Golgi localization (yellow arrowheads) of Fgf3–GFP in expressing cells close to the microlumen (asterisk) and intracellular vesicles in connected non-expressing cells (white arrowheads). No extracellular signal besides microluminal accumulation was detected. Scale bar, 5 µm.

©2014 Macmillan Publishers Limited. All rights reserved

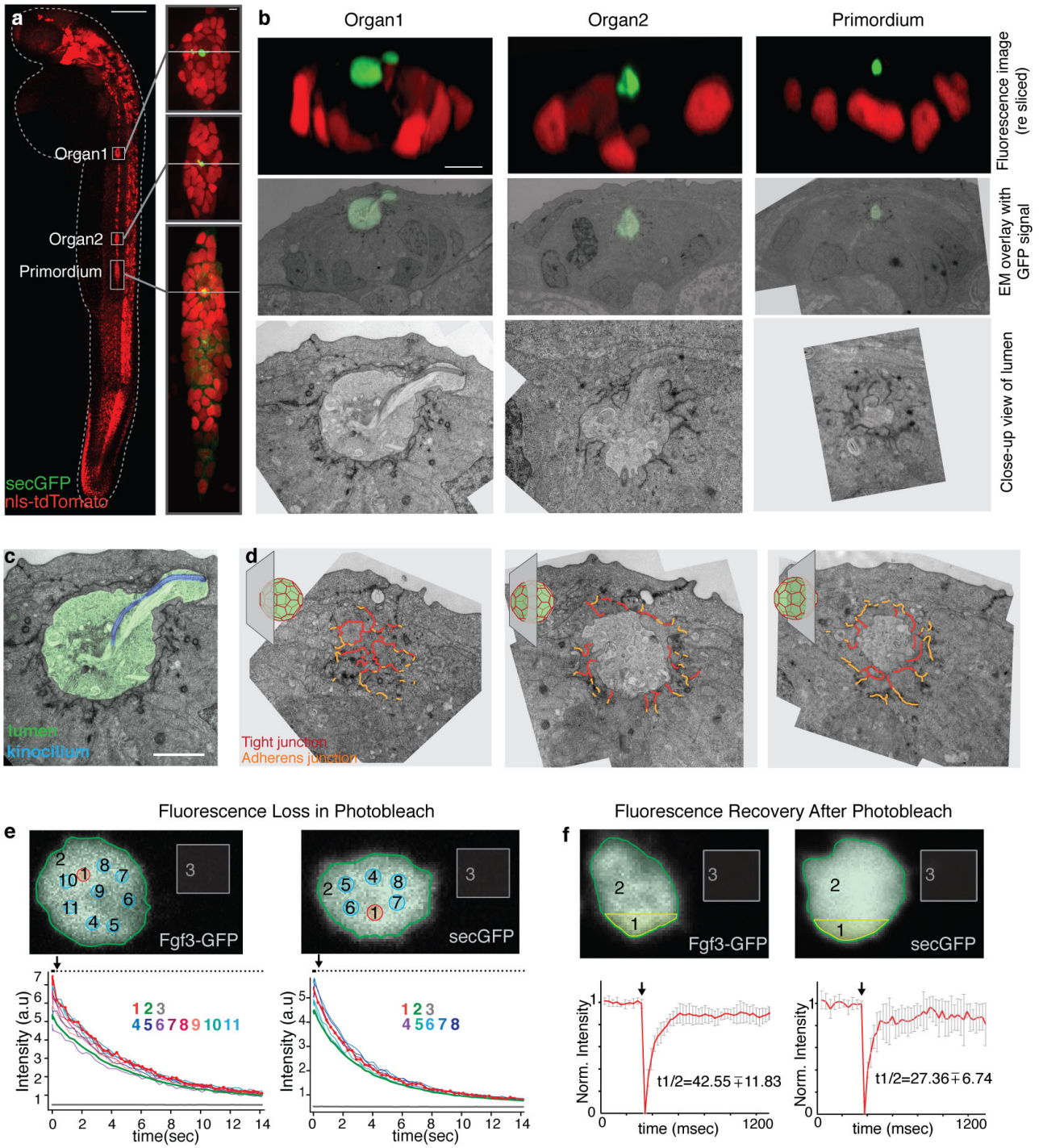

Extended Data Figure 5 | CLEM analysis of microlumen structure and FLIP/FRAP analysis of microluminal pools. **a**, Overview of *lexOP:secGFP*; *cxcr4b:nls-tdTomato* embryo used for CLEM; two organs and migrating primordium were targeted for further processing. Scale bar, 200 µm. **b**, Re-sliced middle section of targeted organ centres, overlay of secGFP signal with corresponding EM slice (scale bar, 5 µm) and close-up view of microlumina. **c**, Close-up view of luminal cavity (green) distorted by kinocilium (blue). **d**, Traced tight junctions (red) and adherens junctions (orange) at three cross-sections of microlumen. **e**, Setup of FLIP experiment on Fgf3–GFP and secGFP pool highlighting repetitively bleached region (0.73 µm diameter, red circle) and regions used for total pool (green circle), background (grey box) and readout (blue circles) measurements. Plots show mean intensity of described ROIs over time. **f**, FRAP experiment on secGFP and Fgf3–GFP pools with a strip ROI. Mean normalized recovery curves (mean ± s.d., $N = 7$) and calculated half time of recovery. Arrow indicates start of bleaching.

©2014 Macmillan Publishers Limited. All rights reserved

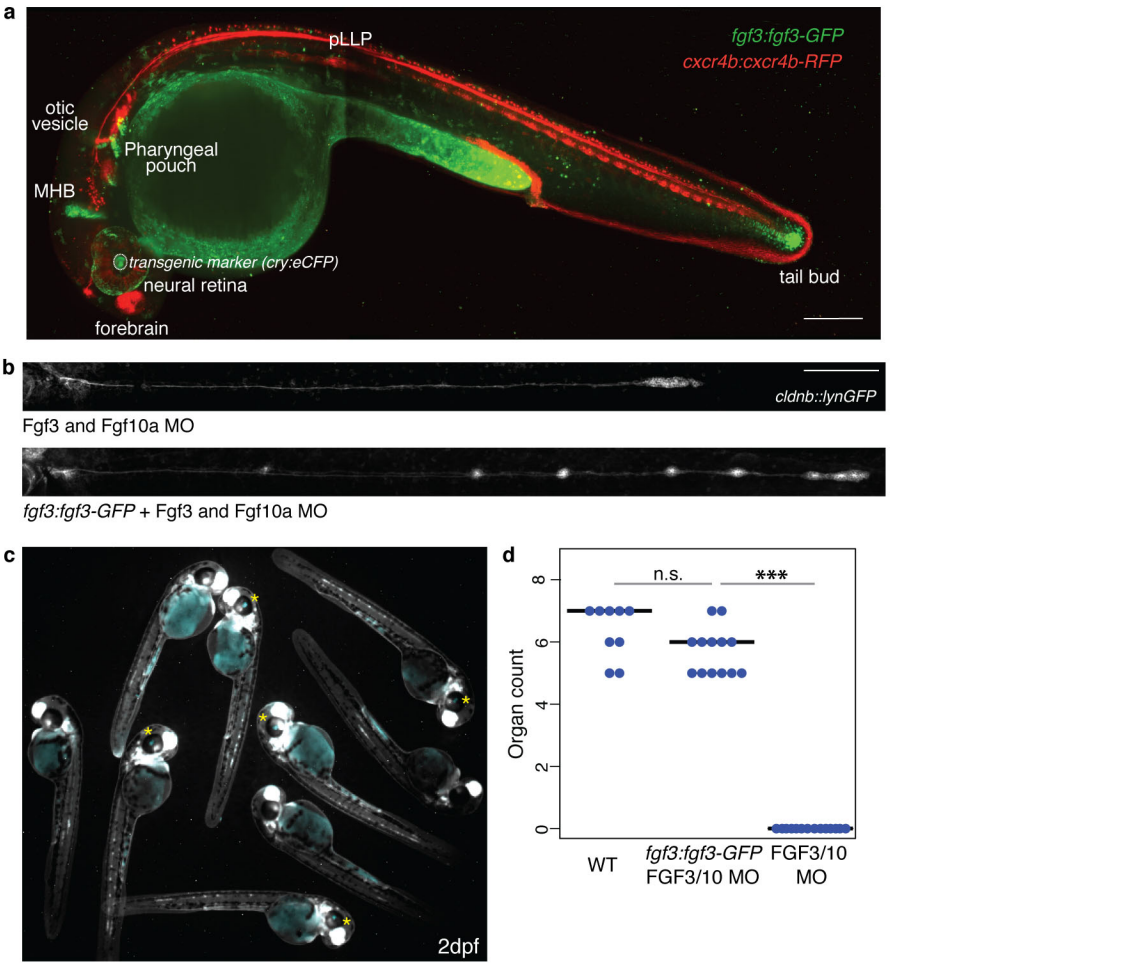

Extended Data Figure 6 | BAC *fgf3:fgf3–GFP* rescues FGF loss of function in lateral line. **a**, BAC *fgf3:fgf3–GFP* line showing expression in known Fgf3 expression domains (28 h.p.f.). Scale bar, 200 µm. **b**, Loss-of-organ deposition phenotype Fgf3/10a morphant embryos (Fgf3/10a MO, upper) is rescued by BAC *fgf3:fgf3–GFP* transgene (lower). **c**, Low-magnification image showing Fgf3/10 morphants, with BAC *fgf3:fgf3–GFP* rescued siblings, distinguished by crystal eye transgene marker (yellow star). Scale bar, 200 µm (**b**). **d**, Quantification of rescue by comparing organ counts of WT, *fgf3:fgf3–GFP* with Fgf3/10 MO background and Fgf3/10a MO alone at 2 d.p.f. ($N_{WT} = 9$, $N_{rescue} = 13$, $N_{Fgf3/10a_MO} = 14$, $P_{WT\text{-}rescue} = 0.09$, $P_{rescue\text{-}Fgf3/10a_MO} = 1.751 \times 10^{-6}$).

©2014 Macmillan Publishers Limited. All rights reserved

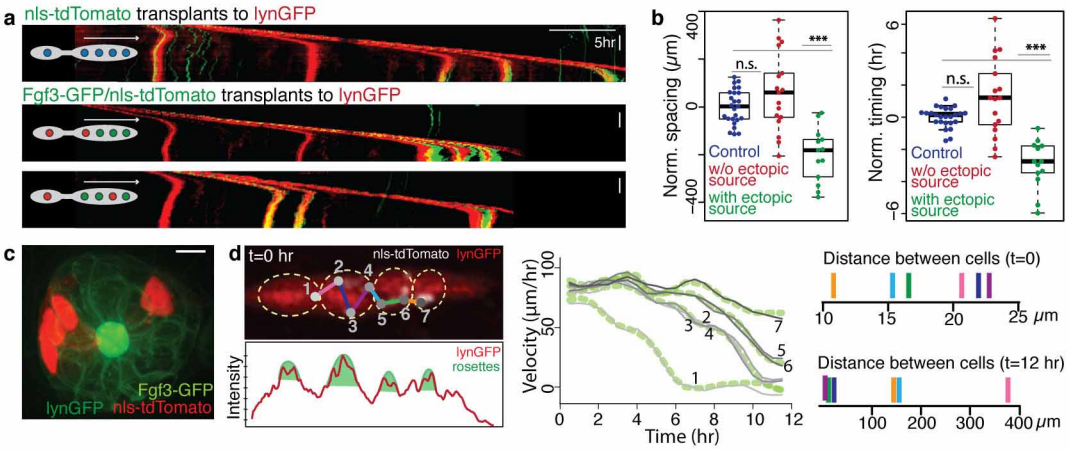

Extended Data Figure 7 | FGF signalling range is restricted to individual organ progenitors. **a**, Kymographs of mosaic Fgf3–GFP expression generated via cell transplantation. *lexOP:fgf3–GFP/cxcr4b:nls-tdTomato*-expressing clones (green) in the *cldnb:lynGFP* line (red) cause rapid arrest of migration. The phenotype only becomes apparent when the organ reaches tissue rear. (Colour code: organs with ectopic FGF source in green; organs without ectopic FGF source in red; organs of control transplants in blue.) Scale bars, 200 μm, 5 h. **b**, Quantification of spacing and deposition timing of organs from mosaic Fgf3–GFP transplants, normalized by mean values of control embryos for each interval ($N_{control} = 7$, $N_{transplants} = 8$, $n_{control} = 25$, $n_{neg} = 17$, $n_{pos} = 13$; spacing: $P_{ctrl-neg} = 0.24$, $P_{ctrl-pos} = 1.43 \times 10^{-5}$, $P_{neg-pos} = 4.40 \times 10^{-5}$; timing: $P_{ctrl-neg} = 0.07$, $P_{ctrl-pos} = 1.23 \times 10^{-6}$, $P_{neg-pos} = 4.09 \times 10^{-5}$). **c**, Close-up view of Fgf3–GFP (green)/nls- tdTomato- (red) expressing clones in *cldnb:lynGFP*- (green) expressing organ, showing cells in different positions feed in the central microlumen. Scale bar, 5 μm. **d**, Tracking of WT transplanted cells (nuclei marked with grey dots and numbered) relative to organ centres in *cldnb:lynGFP* primordium (red). Yellow circles represent each organ unit. Middle panel: calculated velocities for each tracked nucleus (grey lines) and organ centres (green lines) reveal that migration of individual cells is in synchrony with the belonged organ unit independent of their position. Right panel: distance between consecutive tracked cells at the beginning and end of the time-lapse movie shows that initial distance is not a reliable indicator of final cell positions.

©2014 Macmillan Publishers Limited. All rights reserved

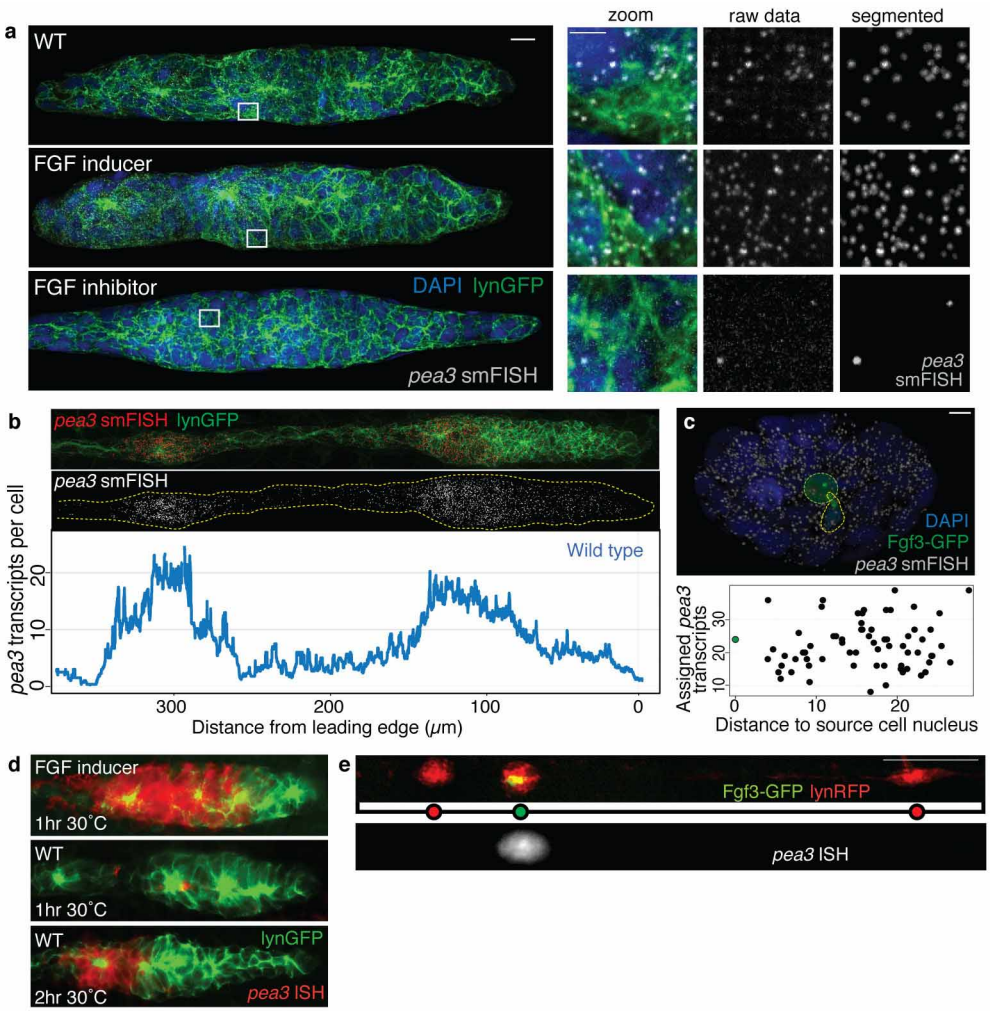

Extended Data Figure 8 | smFISH analysis of FGF target-gene regulation. **a**, *Pea3* smFISH on WT, 15 μM FGF inducer- and 4 μM FGF inhibitor-treated primordia (*cldnb:lynGFP* in green, DAPI staining in blue, *pea3* mRNAs in white), Scale bar, 5 μm. Close-up view of the dashed boxes shown as raw image (middle) and segmented *pea3* transcripts (right). Scale bar, 2 μm. **b**, Image of *pea3* smFISH in WT primordium (above); profile plot shows *pea3* transcripts per cell over distance from leading edge (below). **c**, *Pea3* smFISH in an organ with single Fgf3–GFP-expressing cell. Number of *pea3* transcripts assigned to each nucleus does not show increase towards the expressing cell. Scale bar, 5 μm. **d**, Colorimetric *in situ* hybridization of *pea3* mRNA showing high expression levels upon Fgf3–GFP induction, visible after 1 h colour reaction (30 °C), whereas expression in WT is hardly detectable. However, increasing reaction time reveals *pea3* mRNA signal in WT primordia. **e**, Colorimetric *in situ* hybridization (30 °C, 0.5 h) of *pea3* RNA in mosaic Fgf3–GFP expression shows detectable *pea3* only in the expressing organ. Scale bar, 100 μm.

©2014 Macmillan Publishers Limited. All rights reserved

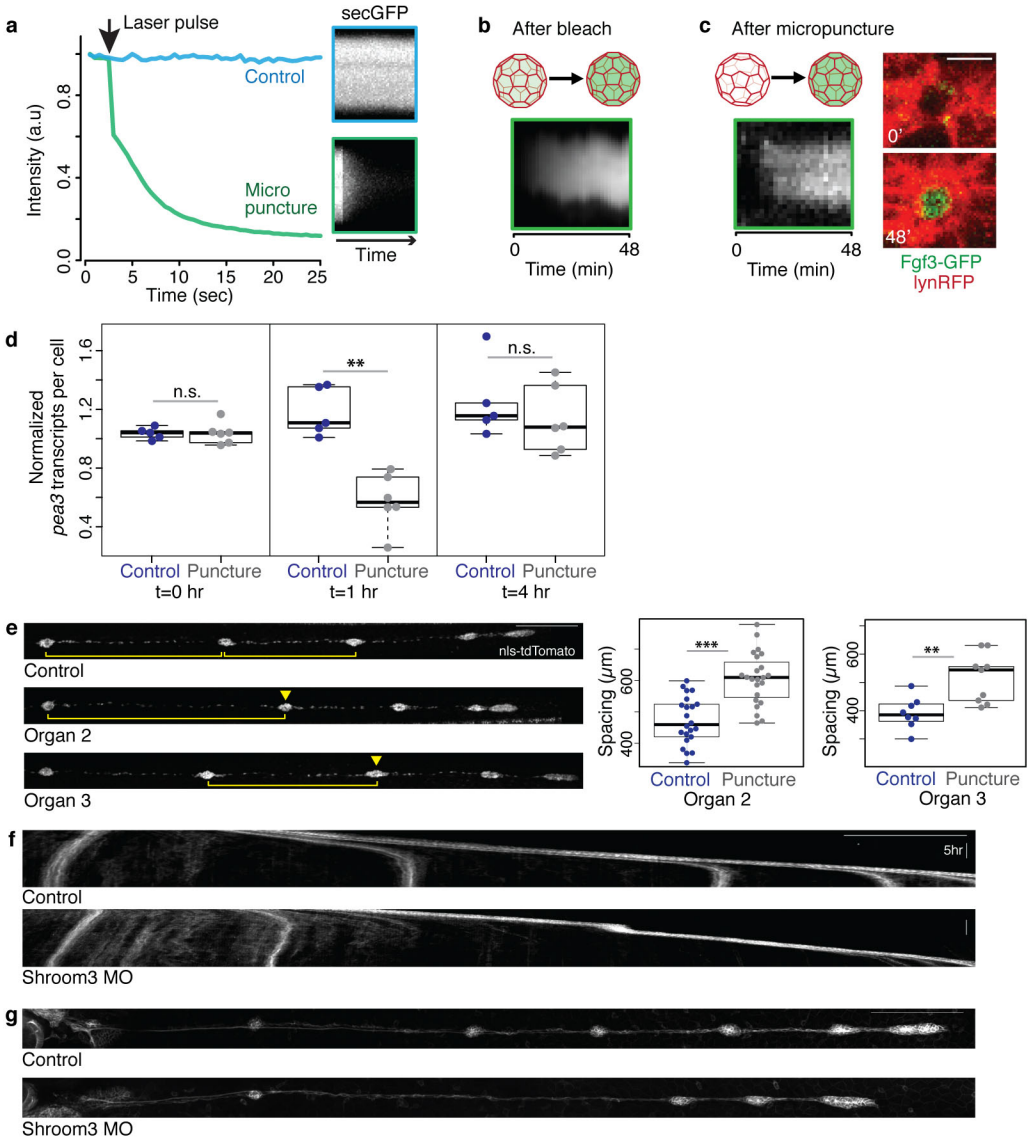

Extended Data Figure 9 | Characterization of luminal integrity and function upon mechanical and genetic perturbation. **a**, Plot of secGFP pool fluorescence intensity upon micropuncture (green). Kymographs show the time-lapse imaging of the secGFP pool used for the plot. **b**, **c**, Luminal Fgf3–GFP signal recovery of whole pool bleached (left) and micro-punctured (right) organs during 48 min of acquisition. Kymographs show time-lapse imaging of Fgf3–GFP pool. Single time points of time-lapse imaging after micro-puncture (right). Scale bar, 5 μm. **d**, Quantification of *pea3* transcript levels at $t = 0$ h, 1 h and 4 h after micropuncture of organ 2 expressing *lexOP:fgf3–GFP*. Unperturbed organ 3 was used for normalization. Comparison of control and punctured organs suggests that *pea3* levels are normal immediately after puncture, are reduced 1 h later and recovered by 4 h ($N_{0\,h\ puncture} = 6$, $N_{0\,h\ control} = 5$, $N_{1\,h\ puncture} = 6$, $N_{1\,h\ control} = 5$, $N_{4\,h\ puncture} = 6$, $N_{4\,h\ control} = 5$, $P_{0\,h} = 0.7922$, $P_{1\,h} = 0.0043$, $P_{4\,h} = 0.4286$). **e**, Organ deposition delay upon lumina micropuncture of secGFP-expressing second and third organs ($N_{ctrl\ second\ organ} = 22$, $N_{puncture\ second\ organ} = 23$, $N_{ctrl\ third\ organ} = 8$, $N_{puncture\ third\ organ} = 9$, $P_{second\ organ} = 6.928 \times 10^{-6}$, $P_{third\ organ} = 0.0061$). Scale bar, 200 μm. **f**, **g**, Shroom3 morphant primordia show intervals with no or delayed deposition. **f**, Kymographs of shroom3 MO and control. Scale bars, 200 μm, 5 h. g, Organ pattern in shroom3 MO and control at 2 d.p.f. Scale bar, 200 μm.

©2014 Macmillan Publishers Limited. All rights reserved

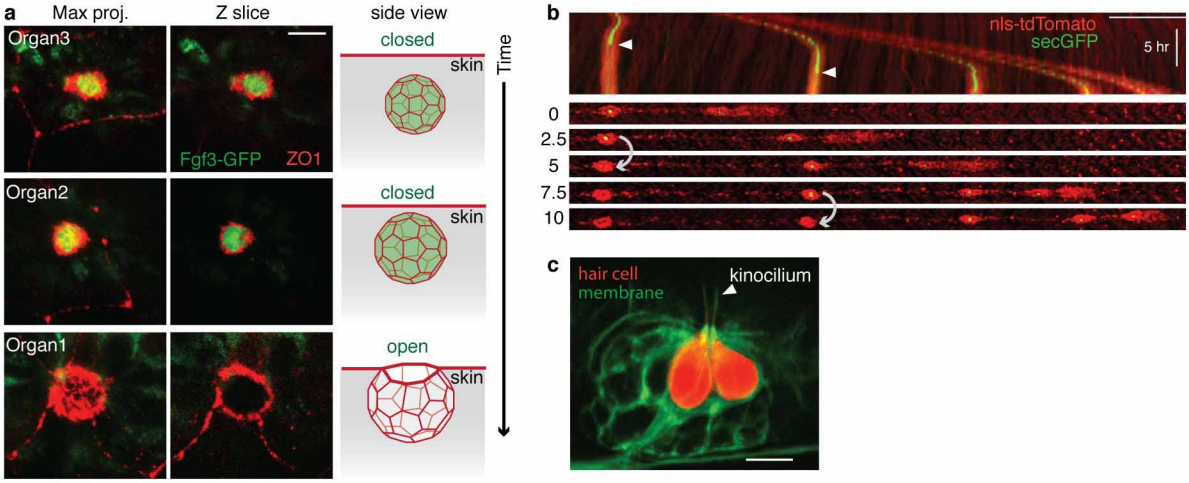

Extended Data Figure 10 | Loss of microlumen pool upon fusion to overlying skin. **a**, Microlumen of maturing organs fuses with the skin and the diffusible content (Fgf3–GFP in green) disappears. Tight junctions marking microlumen and skin borders are revealed by ZO1 immunofluorescence (red). Cartoon displaying the sequence of events (right). Scale bar, 5 µm. **b**, Kymograph and single time-points from time-lapse imaging of secGFP, nls-tdTomato-expressing embryo. SecGFP signal disappears as microlumen opens (arrowheads in kymograph show opening of microlumina). Scale bars, 200 µm, 5 h. **c**, Side view of a maturing organ with kinocilia protruding out of the organ (*cldnb:lynGFP* in green, central cell *atoh1a:tdTomato* in red). Scale bar, 5 µm.

©2014 Macmillan Publishers Limited. All rights reserved